Synaptic Gpr85 influences cerebellar granule cells electrical properties and light-induced behavior.

Romain Darche-Gabinaud[1], Abeer Kaafarani[1], Marine Chazalon[3], Valérie Suain[4], Erika Hendrickx[4], Louise Conrard[4], Anne Lefort[1,5], Frédérick Libert[1,5], Mehmet Can Demirler[1], Serge N. Schiffmann[2,3], David Perez-Morga[4], Valérie Wittamer[1,2], Marc Parmentier[1], Isabelle Pirson[1*].

1 IRIBHM-Jacques E. DUMONT, Université Libre de Bruxelles, route de Lennik 808, 1070 Brussels, Belgium

2 ULB-Neuroscience Institute (UNI), Université Libre de Bruxelles, route de Lennik 808, 1070 Brussels, Belgium

3 Laboratory of Neurophysiology, Université Libre de Bruxelles, route de Lennik 808, 1070 Brussels, Belgium

4 Center for Microscopy and Molecular Imaging, Université Libre de Bruxelles, rue Adrienne Bolland 8, 6041 Gosselies, Belgium

5 BRIGHTcore Facility, IRIBHM-Jacques E. DUMONT, Faculty of Medicine, Université Libre de Bruxelles, route de Lennik 808, 1070 Brussels, Belgium.

***** Corresponding author: Pirson.Isabelle@ulb.be

Abstract

GPR85/SREB2 is an exceptionally well-conserved orphan 7TM receptor with unclear biological attributes. In this study, we used several zebrafish genetic models to investigate Gpr85 properties and functions throughout development and adulthood. We describe that, like in mammals, *gpr85* is expressed by various neuronal populations throughout zebrafish development and adulthood in the central nervous system, retina and intestine. The overexpression of a fluorochrome-tagged version of the receptor in *gpr85*-expressing neurons provides the first *in vivo* evidence that Gpr85 is enriched at the synaptic level in the brain and retina. Transcriptomic analysis of Gpr85 knock-out zebrafish cerebellar granule cells revealed changes in gene expression related to enhanced neuronal activity. Further investigations using *ex vivo* cerebellar slices demonstrate that the electrophysiological activity of Gpr85 deficient granule cells are increased. We also observed that Gpr85 deficient larvae exhibit enhanced light-triggered startle responses in dark/light paradigm behavioral experiments. Altogether, our results provide evidence that, in zebrafish, Gpr85 is enriched at the synaptic level *in vivo* and influences granule cell electrophysiological properties as well as light-triggered motor responses.

Keywords: behavior/brain/SREB2/synapse/zebrafish

Introduction

GPR85 is classified as a class A G protein-coupled receptor (GPCR). It belongs to the Super Conserved Receptors Expressed in Brain (SREB) subfamily, which includes GPR27 (SREB1), GPR85 (SREB2) and GPR173 (SREB3). In mammals, *GPR85* is broadly expressed in the brain, with the strongest expression in the cerebellum (Hellebrand *et al*,

2001, 2000; Matsumoto *et al*, 2005). It is also found in the pituitary gland, retina, intestine, and testis (Matsumoto *et al*, 2000; Regard *et al*, 2008; Ito *et al*, 2009). Interestingly, *Gpr85* transcripts were already detected during early mouse and zebrafish (*Danio rerio*) development (Hellebrand *et al*, 2001; Thisse & Thisse, 2004). Strikingly, GPR85 is exceptionally well-conserved among mammals, with an identical protein sequence between human, primates, and rodents, while being absent in invertebrates (Hellebrand *et al*, 2000). In zebrafish, an evolutionarily more distant vertebrate model, the receptor nevertheless shares 93.8% amino acid identity with its human counterpart (https://blast.ncbi.nlm.nih.gov/Blast.cgi). This strong conservation across vertebrates has drawn significant interest and suggests that GPR85 plays an important role in physiological processes. However, GPR85 remains an orphan receptor, as its natural ligands have not been identified (http://www.guidetopharmacology.org). In addition, no constitutive activity of the receptor has yet been conclusively demonstrated. The lack of pharmacological characterization has so far hindered a complete understanding of its biological functions.

From a pathological perspective, a correlative study has shown an association between two *GPR85* single nucleotide polymorphisms (SNPs) and schizophrenia, leading to the proposal of categorizing GPR85 as a schizophrenia risk factor (Matsumoto *et al*, 2008; Chen *et al*, 2012). Additionally, two *GPR85* missense mutations were found in patients with Autism Spectrum Disorder (ASD) (Fujita-Jimbo *et al*, 2015). *GPR85* expression was also shown to be repressed by an edited miRNA (A to I, hsa-mir-376a-5p) that is enriched in ASD patients (Wu *et al*, 2022). Despite these findings, the involvement of the receptor in the etiology of complex neurological and developmental disorders, such as autism and schizophrenia, remains to be fully elucidated.

Studies have documented the regulation of *Gpr85* expression following treatment of neurons with excitatory (kainic acid, picrotoxin) or inhibitory (TTX) drugs *in vitro* and *in vivo* (Jeon *et*

al, 2002; Jin *et al*, 2018a). Later on, *Gpr85* was shown to be upregulated in SHANK3-overexpressing mice in several regions of the adult brain (Jin *et al*, 2018b, 2018a). These mice display manic-like behavior and spontaneous seizures, associated with altered excitatory/inhibitory balance, suggesting that *Gpr85* expression is modulated by neuronal activity and may regulate it. Using neuronal cell cultures, Fujita-Jimbo *et al*, (2015) reported an interaction between GPR85 and PSD-95, suggesting that the receptor localizes at the postsynaptic level of excitatory chemical synapses. The function of GPR85 in brain physiology has been investigated using two complementary mouse models. Constitutive GPR85 knock-out (KO) mice exhibited increased brain weight and improved spatial memory while mice overexpressing the receptor in postnatal forebrain neurons displayed reduced brain weight alongside social and cognitive defects (Matsumoto *et al*, 2008; Chen *et al*, 2012). Additional studies using these mutants have led the authors to propose GPR85 as a negative regulator of adult neurogenesis in the mouse hippocampus, subsequently influencing learning and memory (Chen *et al*, 2012). However, the role of GPR85 in adult neurogenesis has not been confirmed in further studies. Despite recent advances, the biological attributes and roles of GPR85 remain unclear. In the present work, we aimed to further investigate the properties and functions of the receptor *in vivo*. To achieve this, we took advantage of zebrafish as a powerful genetic model to generate Gpr85-KO, *gpr85* reporter and transgenic lines. The phenotypical characterization of the reporter line confirmed and refined the expression pattern of *gpr85* during zebrafish development and adulthood. We also assessed Gpr85's subcellular localization in the retinal and cerebral neurons. Finally, we investigated the physiological impact of Gpr85 deficiency and demonstrated that Gpr85 influences adult cerebellar neuronal activity and passive electrophysiological properties, as well as larvae light induced behavior. Altogether, our results reveal that Gpr85 is a synaptic membrane receptor

in vivo and suggest that it contributes to the modulation of neuronal activity, thereby influencing stimulus-induced behavioral responses.

Results

Characterization of newly generated knock-in zebrafish *gpr85* reporter lines

Firstly, to define the tissues expressing *gpr85* in zebrafish embryos, we performed whole-mount *in situ* hybridization (WISH) at different developmental stages from 1 to 6 days post-fertilization (dpf). The signal emerged at 1 dpf in the telencephalic and ventral midbrain regions, thereafter expanding to the entire brain by 6 dpf (Appendix Fig. S1A). Transcripts were also observed in the retina of 3 dpf zebrafish larvae (Appendix Fig. S1B). To better define *gpr85* expression, we generated a zebrafish reporter line using CRISPR/Cas9 technology with targeted integration repair (Wierson *et al*, 2020; Welker *et al*, 2021). The GAL4 open reading frame was inserted downstream of the endogenous *gpr85* start codon, creating a receptor loss-of-function allele (Appendix Fig. S1C). The correct insertion of the GAL4 cassette at the *gpr85* locus was validated using PCR genotyping (Appendix Fig. S1D) and Sanger sequencing. We then introduced the *gpr85*^{GAL4} allele into either the *Tg(UAS:GFP-CAAX)*^{m1230} or *Tg(UAS:LifeAct-eGFP)*^{mu271} backgrounds. Phenotypic observations of these two lines did not reveal any developmental or adult behavioral defects in the heterozygous *gpr85*$^{GAL4/+}$ state. Adult zebrafish were fertile, and their offspring followed a mendelian inheritance ratio. All observations described hereafter were consistent across both lines.

We first characterized the general expression profile of the GFP-CAAX reporter during the embryonic development of *gpr85*$^{GAL4/+}$, *Tg(UAS:GFP-CAAX)* individuals. Whole body imaging of live embryos revealed that the GFP signal emerged at 1 dpf in the telencephalic

and ventral midbrain regions (Fig. 1A-B). At 2 dpf, the expression expanded to include forebrain and midbrain (Fig. 1C), persisting through the end of embryogenesis (3 dpf; Fig. 1D) and into post-embryonic stages (6 dpf; Fig. 1E). Consistent with WISH experiments, GFP was detected in the retina (Fig. S1E-H''). Using immunodetection on coronal sections of 3 dpf embryos (Appendix Fig. S1E-F'') and 6 dpf (Appendix Fig. S1G-H'') larvae, revealed GFP-positive (GFP^+) cells predominantly in the ganglion cell layer (GCL) and inner nuclear layer (INL), but not in the photoreceptor layer (ONL) (Appendix Fig. S1F; H). GFP was also detected in the spinal cord (Fig. S1I-J''), though this have not been detectable with the less sensitive WISH method (Fig. S1A-B). We observed GFP expression in both the ventral and dorsal regions of the developing spinal cord of 3 dpf embryos (Appendix Fig. S1I-I'') and 6 dpf larvae (Appendix Fig. S1J-J'').

Furthermore, we observed GFP signal in the intestine of 6 dpf larvae, where specific cells were labelled all along the tract (Appendix Fig. S2A-B). Using *gpr85*$^{GAL4/+}$, *Tg(UAS:GFP-CAAX, NBT:DsRed)* fish, we identified neurons ($DsRed^+$ cells) as the GFP^+ cells in the developing intestine of 6 dpf zebrafish (Appendix Fig. S2C-D). We then pursued the analysis of *gpr85* expression pattern in the developing brain, where it was already highly expressed by 2 dpf.

Gpr85 is broadly expressed in zebrafish brain neurons at the end of embryogenesis.

To delineate more precisely the anatomical structures of the developing zebrafish brain that express *gpr85*, we performed anti-GFP immunodetection on coronal sections of 3 and 6 dpf *gpr85*$^{GAL4/+}$, *Tg(UAS:Lifeact-eGFP)* embryos. At 3 dpf, Lifeact-eGFP expression was detected throughout the brain (Fig. 1F-I). *Gpr85*-reporter expression was observed in the olfactory bulb and subpallium but notably, no signal was detected in the olfactory epithelium at this stage (Fig. 1F'). *Gpr85*-reporter expression was observed in cell clusters from left and

right habenula (Fig. 1G'). In more caudal brain regions, Lifeact-eGFP^{+} cells were scattered throughout the brain parenchyma (Fig. 1H'-I').

To confirm the neuronal identity of Lifeact-eGFP^{+} cells, co-immunostaining was performed with HuC, a pan-neuronal marker during zebrafish embryogenesis (Kim *et al*, 1996; Park *et al*, 2000). All Lifeact-eGFP^{+} cells were also positive for HuC (Fig. 1J-M) except for a few Lifeact-eGFP^{+}/HuC^{-} cells which were observed in the midbrain ventral neuronal progenitor/precursor zone (Fig. EV1A-A''', arrowheads). These cells are likely post-mitotic neuronal precursors migrating toward the developing brain parenchyma, as no PCNA^{+}/Lifeact-eGFP^{+} cells were found in this region (Fig. EV1B-C'', arrowheads). Thus, at the end of embryogenesis, Lifeact-eGFP^{+} cells in the brain can likely be classified as maturing neurons.

A similar expression pattern of the *gpr85* reporter was observed in our *gpr85*$^{GAL4/+}$*, Tg(UAS:Lifeact-eGFP)* line at 6 dpf in the hypothalamus (Fig. EV1D), olfactory bulb, pallium, subpallium (Fig. EV1E), habenula (Fig. EV1F; H), torus longitudinalis, optic tectum, cerebellum, and medulla oblongata (Fig. EV1G) (Shainer *et al*, 2023; Data ref: Shainer *et al*, 2023).

We then compared our *gpr85* expression data in embryos with a previous zebrafish brain single-cell transcriptomic dataset named "Daniocell", which covers zebrafish development from 3 to 120 hours post fertilization (hpf) (Ja *et al*, 2018; Sur *et al*, 2023; Data ref: Sur *et al*, 2023). Analysis of *gpr85* expression dynamics, as confirmed with our *gpr85*$^{GAL4/+}$ reporter lines, showed that *gpr85* transcripts were undetectable before the mid-segmentation stage (14-21 hpf) (Appendix Fig. S3A). Afterwards, transcripts were observed in the neural system, eye and spinal cord throughout embryonic and post-embryonic development (Appendix Fig. S3B). Expression onset occurred in neurons of the developing forebrain, as well as motor neurons and interneurons in the spinal cord (Fig. S3C). At mid-segmentation, *gpr85*-

expressing neurons were identified in the pallium and ventral forebrain/diencephalon (Fig. S3C). Later during embryonic development, *gpr85* expression expanded to other brain structures, where it was observed in various neuronal cell types, including GABAergic, glutamatergic, glycinergic and dopaminergic neurons. The expression of *gpr85* was detected in neuronal subpopulations of the retina INL and GCL, consistent with our observations (Appendix Fig. S1F and H), emerging from 36 hpf, in amacrine cells (ACs) and in ON/OFF bipolar cells (BPCs). Finally, these transcriptomic data showed no *gpr85* expression in neural progenitors, endothelial cells, or immune cells of the central nervous system (CNS). Taken together, these data suggest that our newly generated *gpr85*^{GAL4} reporter lines provide robust models for identifying and studying *gpr85*-expressing cell populations in the zebrafish CNS and retina.

Gpr85 expression is maintained in the brain, retina and intestine of adult zebrafish

The expression profile of *gpr85* in the adult zebrafish brain has been previously documented by others through qPCR analysis (Breton *et al*, 2023), though with limited spatial resolution. Taking advantage of our *gpr85* reporter lines, we further characterized the anatomical distribution of *gpr85*-expressing cells in the adult zebrafish brain. We first performed tissue clearing of *gpr85*$^{GAL4/+}$, *Tg(UAS:Lifeact-eGFP)* adult brains and analyzed sagittal and coronal sections from *gpr85*$^{GAL4/+}$, *Tg(UAS:GFP-CAAX*) brains. As during development, GFP^{+} cells were observed in various regions of the adult brain (Fig. 2A). In the hindbrain, the highest expression was observed in the cerebellum (Ce; Fig. 2A, B-E'), with scattered GFP^{+} cells in the medulla oblongata (MO; Fig. 2A). In the midbrain, a strong signal was detected in the torus longitudinalis (TL; Fig. 2A, F-G') and the optic tectum (TeO; Fig. 2A; Fig. EV2C-C'). In the forebrain, GFP^{+} cells were scattered in the olfactory bulb (OB; Fig. 2A), pallium/subpallium of the telencephalon (Tel; Fig. 2A) and the hypothalamus (H; Fig. 2A). In

the hypothalamus, a strong GFP signal was observed in the posterior recess (Fig. 2A; Fig. EV2D-E'). In line with our previous observations in embryos, clusters of GFP+ cells were detected in right and left habenula (Ha; Fig. 2A and H-H'). Of note, while a strong GFP signal was observed in the pituitary (Fig. EV2A-B'), GFP^+ cells were sparse, suggesting that the signal mainly originates from neuronal projections rather than intrinsic pituitary cells. Overall, strong *gpr85* expression was thus identified in the habenula, hypothalamus, torus longitudinalis, and cerebellum of the adult zebrafish brain, consistent with developmental patterns.

In addition to the brain, we investigated *gpr85*-reporter expression in the intestine. Using the *gpr85*$^{GAL4/+}$, *Tg(UAS:GFP-CAAX, NBT:DsRed)* line, we confirmed the presence of GFP^+/$DsRed^+$ neurons in the adult intestine (Fig. S2E). In addition, sparse GFP^{low}/$DsRed^-$ cells were scattered within the intestinal villi (Fig. S2F-G). Since Gpr85 expression has been previously reported in the human testis (Matsumoto *et al*, 2000), we also investigated its presence in zebrafish gonads. In the testis, GFP signal was detected in all cells (Fig. S2H-H'), whereas no GFP^+ cells were observed in the ovaries. Consistent with findings from embryonic stages, GFP^+ cells were also detected in the INL and the GCL of the adult retina (Fig. 3A-A'). Taken together, our observations reveal that the distribution of *gpr85*-expressing cells is conserved from the end of embryogenesis to adulthood across the brain, retina and intestine.

Gpr85 receptor localizes to synapses in the retina and brain

To gain insight into the biological function of Gpr85, we characterized its subcellular localization *in vivo*, with a focus on neurons of the zebrafish brain and retina. A previous *in vitro* study suggested an interaction between GPR85 and neuroligin-bound PSD-95, a postsynaptic marker of excitatory synapses (Fujita-Jimbo *et al*, 2015). Based on this, we

hypothesized that Gpr85 could function as a receptor in zebrafish chemical synapses. To address this, we used our *gpr85*$^{GAL4/+}$ line to overexpress the Gpr85 receptor fused to either eGFP or mCherry at its C-terminal end. Both *gpr85*$^{GAL4/+}$, *Tg(UAS:zGpr85-eGFP)* and *gpr85*$^{GAL4/+}$, *Tg(UAS:zGpr85-mCherry)* lines were fertile and did not exhibit developmental defects. No ectopic expression was observed but both lines displayed a mosaic expression of the chimeric receptors, as compared to the Lifeact-eGFP and GFP-CAAX lines.

Firstly, we observed the subcellular localization of Gpr85 receptor in the retina. Coronal sections of the retina from *gpr85*$^{GAL4/+}$, *Tg(UAS:zGpr85-eGFP)* fish revealed zGpr85-eGFP^{+} ACs (Fig. 3B and F) and BPCs (Fig. 3D and H) during development and adulthood. In ACs, the zGpr85-eGFP signal was localized in the soma (Fig. 3B and F, black arrowhead) and dendritic arborization of the cells within the IPL at both 6 dpf (Fig. 3B) and 6 months post fertilization (mpf) (Fig. 3F). In BPCs, the zGpr85-eGFP signal was also observed in the soma (Fig. 3D, black arrowhead) and neurites/terminals in larvae IPL (Fig. 3D) while only found in the IPL of adult zebrafish (Fig. 3H). The dendritic arborization of BPCs was essentially devoid of zGpr85-eGFP. The co-immunostaining for αRibeye-a, a marker of presynaptic ribbon synapse compartments showed that the zGpr85-eGFP signal was enriched at the postsynaptic sites of ribbon synapses in the dendritic arborization of developing (Fig. 3C-C'', white arrowheads) and adult (Fig. 3G-G'', white arrowheads) ACs. In developing (Fig. 3E-E'', white arrowheads) and adult (Fig. 3I-I'', white arrowheads) BPCs, on the contrary zGpr85-eGFP displayed a strong signal at the level of the Ribeye-a^{+} presynaptic terminals of ribbon synapses. Hence, the distribution of zGpr85-eGFP in ACs and BPCs provides the first *in vivo* evidence that Gpr85 is enriched at both pre- and postsynaptic levels in ribbon synapses of the IPL of the developing and adult retina. Given that Gpr85 is a 7TM receptor, it was anticipated to localize at the plasma membrane *in vivo*. However, no direct evidence of such localization had been reported previously. Using *gpr85*$^{GAL4/+}$, *Tg(UAS:zGpr85-mCherry)*

larvae, we investigated the distribution of the receptor by electron microscopy using immunogold staining. The initial characterization of the retinal structure revealed the ribbon terminals within the IPL (Fig. 3J-K, yellow). Presynaptic compartments were identifiable due to the presence of presynaptic vesicles (Fig. 3L-M, black arrows) while postsynaptic densities were identified as thick and electron-dense portions of the membranes (Fig. 3L-M, white arrowheads). Ribeye-a localization in presynaptic terminals was confirmed (Fig. 3N-P). As expected, zGpr85-mCherry exhibited localization at the plasma membrane in the IPL (Fig. 3Q-S).

Secondly, we studied the subcellular localization of the chimeric receptor in the developing and adult brain, using the *Tg(UAS:FinGR(PSD)-GFP)* and *Tg(UAS:FinGR(GPHN)-mCherry)* reporter lines to discriminate between excitatory and inhibitory synapses, respectively (Son *et al*, 2016). These reporter transgenes were respectively introduced into our *gpr85*$^{GAL4/+}$, *Tg(UAS:zGpr85-mCherry)* or *Tg(UAS:zGpr85-eGFP)* stable lines and co-immunostaining was performed on 6 dpf coronal sections and adult sagittal sections of the brain. As in the retina, zGpr85-eGFP^{+} and zGpr85-mCherry^{+} puncta were identified in neuronal projections at both larval and adult stages (Fig. 4). We observed both zGpr85-mCherry^{+}/PSD^{+} (Fig. 4A,B, white arrowheads) and zGpr85-eGFP^{+}/GPHN^{+} (Fig. 4C,D, white arrowheads) synapses in multiple regions of the developing and adult brain, including the telencephalon, hypothalamus, optic tectum, and cerebellum. Overall, our observations provide the first *in vivo* evidence that Gpr85 is a receptor present at the plasma membrane of chemical synapses in the retina and CNS throughout zebrafish development and adulthood.

Gpr85 is dispensable for the development, viability, and formation of excitatory inputs of *gpr85*-expressing optic tectal neurons.

Our results showed that *gpr85* is expressed by various differentiating neuronal subpopulations during early zebrafish brain development. In addition, we provided evidence that Gpr85 is a synaptic membrane receptor *in vivo*. These observations prompted us to investigate whether Gpr85 plays a role in the development and/or maturation of *gpr85*-expressing neurons.

To address this, we generated a complementary constitutive Gpr85-KO model (*gpr85*$^{\Delta 4/\Delta 4}$) (Appendix Fig. S4A). Similar to the *gpr85*$^{GAL4/GAL4}$ line, homozygous mutants were viable, fertile, and displayed no noticeable developmental defects (Appendix Fig. S4B,C). The offspring of these mutants followed a Mendelian inheritance ratio (Appendix Fig. S4D). While a previous study reported increased brain weight in GPR85-KO mice (Matsumoto *et al*, 2008), we observed no significant differences in body length or in the wet brain weight-to-body length ratio in either of the Gpr85-KO zebrafish models (Appendix Fig. S4E,F). Nevertheless, we observed that *gpr85* transcript levels were approximately twice as high in both Gpr85-KO models compared to WT 6 dpf larvae (Appendix Fig. S4G), suggesting that the absence of functional Gpr85 triggers upregulation of the gene and/or increases the stability of its transcripts. To further investigate the impact of Gpr85-KO on the development of *gpr85*-expressing neurons, we used *gpr85*$^{GAL4/\Delta 4}$, *Tg(UAS:FinGR(PSD)-GFP)* larvae to quantify the developing optic tectal *gpr85*-expressing neurons in the *stratum paraventriculare* (SPV) and their excitatory inputs within the neuropil. The neuropil, almost devoid of neuronal soma, exhibits a uniform distribution of excitatory inputs at 6 dpf (Appendix Fig. S4H-M). We observed no significant changes in the density of FinGR(PSD)-GFP^{+} cells in the SPV of 6 dpf larvae in the Gpr85-KO larvae compared to controls (Appendix Fig. S4I,J). Similarly, the density of FinGR(PSD)-GFP^{+} synaptic inputs within the tectal neuropil remained unaffected in whole-mount immunostaining of Gpr85-KO larvae (Appendix Fig. S4L,M). Hence, these

results show that Gpr85 is dispensable for the development, viability and formation of excitatory inputs in *gpr85*-expressing neurons during zebrafish development.

Transcriptomic analysis of Gpr85-KO cerebellar granule cells reveals changes in genes related to neuronal activity.

Although Gpr85 appears dispensable for the development of *gpr85*-expressing neurons and developmental synaptogenesis, it may influence neuronal homeostasis and/or synaptic activity. To explore the potential impact of constitutive Gpr85 deficiency on adult *gpr85*-expressing neurons, we conducted single-cell RNA sequencing (scRNAseq) on eGFP^{+} sorted cells from the adult brains of *gpr85*$^{GAL4/GAL4}$, *Tg(UAS:Lifeact-eGFP)* and *gpr85*$^{GAL4/+}$, *Tg(UAS:Lifeact-eGFP)* zebrafish. After filtering, data from both genotypes were merged for clustering, which identified 11 distinct clusters under both control and knock-out conditions (*gpr85*$^{GAL4/+}$, Ctl, n = 4219 cells; *gpr85*$^{GAL4/GAL4}$, KO, n = 3341 cells) (Fig. 5A). As expected, most cells (96%) exhibited expression of the eGFP transgene (Fig. 5B) which was 2.4 times more abundant in Gpr85-KO cells carrying two GAL4 alleles (Table EV1). *Gpr85* transcripts were detected, though not in all cells (Fig. 5B), likely due to expression levels below the detection threshold of the sequencing method and/or dynamic expression patterns not captured by the stable eGFP reporter. Unlike our RT-qPCR findings at 6 dpf, this adult dataset showed no global or cluster-specific upregulation of *gpr85* transcripts (Table EV1).

All clusters, except cluster 9, displayed neuronal identities, expressing the pan-neuronal markers *elavl3* and *rbfox3a* (Fig. 5B). Based on *gad1a* expression, we observed that 98% of the cells were non-GABAergic neurons. Cluster 9 was identified as non-neuronal, expressing leukocyte and microglial markers such as *cd74b*, *mhc2a*, *apoeb* (Fig. EV3 A, B) and *mpeg1.1* (Table EV1). Clusters 0–6 were identified as cerebellar granule cells (GCs) based on markers like *vsnl1a* and *pde1a* (Fig. 5B, Fig. EV3A,B), while lacking markers for Purkinje,

eurydendroid, Golgi and stellate cells (*gad1a, calb2a, aldoca, ca8, slc1a3b, fabp7a*) (Fig. EV3C). Cluster 8 was composed of ventral telencephalon neurons, cluster 10 of dorsal pallium neurons characterized by expression of *eomesa* (Fig. EV3B, Table EV1), and cluster 11 of *kiss1*+ neurons from the ventral habenula (Fig. EV3B, Table EV1). The majority of cells in the dataset (90%) were thus identified as GCs.

To identify transcriptional changes resulting from the loss of Gpr85, we focused on cerebellar GCs from clusters 0 to 6 to assess differential expressed genes (DEGs). Firstly, we selected genes with a fold change (FC) ≥ 2, adjusted p-value $< 10^{-4}$ and expressed by $\geq 6\%$ of cells. We identified 27 upregulated and 23 downregulated genes (Fig. 5C). The most upregulated gene was the ornithine decarboxylase antizyme *oaz2b* (FC = 5.13), and *oaz1a,* was also among the upregulated genes. The histone-like *hist1h4l.18* was the most downregulated gene. Remarkably, seven of the most upregulated DEGs were identified as immediate early genes (IEGs): *npas4a*, *fosab*, *egr1*, *egr4*, *junbb*, *gadd45ba* and *ier2b* (Fig. 5C). Basal expression of *fosab* and *egr1* transcription factors in the adult zebrafish cerebellum has been reported (Kühn and Köster, 2010; Kress and Wullimann, 2012). Consistent with this, several of these IEGs were defined as main markers specifying cluster 2, confirming the existence of a GC subpopulation expressing multiple IEGs in basal conditions (Fig. 5D, Fig EV3A, B, Appendix Table S1, Table EV1). Upregulated genes also included three genes encoding proteins involved in neuronal activity and excitability, a potassium voltage-gated channel (*kcnh3*), an ATPase Na^+/K^+ transporting subunit (*atp1b1b)* and the gamma-aminobutyric acid type A receptor subunit delta (*gabrd*) (Fig. 5C). These observations led us to further investigate the list of DEG focusing on genes related to neuronal activity and/or excitability. In total, we observed ten documented IEG which displayed a significant upregulation in the Gpr85-KO GCs, mostly observed within the IEG^+ GC cluster 2 (Fig. 5D, E, Appendix Table S1, Table EV1, FC > 1.7, adjusted p-value $< 10^{-11}$). In addition, there was upregulation of 11

genes related to neuronal activity-dependent exocytosis, and 8 genes encoding ATPase Na^+/K^+ exchangers or voltage-dependent channels (Fig. 5D, Appendix Table S1, Table EV1, FC > 1.4, adjusted, p-value < 10^{-4}). Unlike the IEGs, upregulation of the channels was broadly distributed across GCs clusters, as exemplified with *npas4a*, *chga* and *atp1b2a* (Fig. 5E). Altogether, these observations indicate that *gpr85* is predominantly expressed in cerebellar GCs within the adult zebrafish brain. The absence of Gpr85 alters the transcriptional profile of these neurons, particularly genes associated with neuronal activity and excitability suggesting a role for Gpr85 in modulating cerebellar GCs electrophysiological activity.

Spontaneous activity of adult cerebellar Gpr85-KO GCs is increased *ex vivo*.

Based on our transcriptomic analysis, we hypothesized that the electrophysiological properties of cerebellar GCs might be altered in Gpr85-KO models. To investigate this, we conducted electrophysiological recordings on *ex vivo* horizontal cerebellar slices from adult *gpr85*$^{GAL4/+}$ (or *gpr85*$^{GAL4/GAL4}$), *Tg(UAS:Lifeact-eGFP)* zebrafish (Fig. 6A). Recordings focused on *gpr85*-expressing GCs (eGFP$^+$), to assess their spontaneous neuronal activity and passive membrane properties (Fig. 6A-C). In both conditions, cell-attached recordings exhibited GCs with either no (*gpr85*$^{GAL4/+}$: 17/30, 57% vs *gpr85*$^{GAL4/GAL4}$: 10/25, 40%) or with a spontaneous activity (*gpr85*$^{GAL4/+}$: 13/30, 43% vs *gpr85*$^{GAL4/GAL4}$: 15/25, 60%) (Fig. 6A). Among the recorded active neurons, we observed that the Gpr85-KO GCs firing rate was significantly increased, as compared with the Gpr85-Ctl active GCs (Fig. 6B, Hz, *gpr85*$^{GAL4/+}$, 4.69 ± 1.24 vs *gpr85*$^{GAL4/GAL4}$, 12.62 ± 3.24, p = 0.035, t-test). This observation provides the first evidence that Gpr85 could be involved in regulating the excitability of the adult cerebellar GCs. Next, we investigated the passive membrane properties of neurons using a whole-cell patch voltage clamp configuration. While the capacitance (Cm) was not significantly different between our groups (Fig. 6C), we observed a significant increase in membrane resistance

(Rm) in Gpr85-KO GCs (Cm: *gpr85*$^{GAL4/+}$, 2.46 ± 0.25 pF vs *gpr85*$^{GAL4/GAL4}$, 2.58 ± 0.34 pF, p = 0.913, M-W test; Rm: *gpr85*$^{GAL4/+}$, 3079 ± 188 MΩ, n = 26 vs *gpr85*$^{GAL4/GAL4}$, 4663 ± 554 MΩ, p = 0,011, t-test). This was not accompanied by significant changes in the membrane time constant (mS, *gpr85*$^{GAL4/+}$, 7.47 ± 0.93 ms vs *gpr85*$^{GAL4/GAL4}$, 10.81 ± 1.65 ms, p = 0.172, M-W test) (Fig. 6C). Altogether, these results indicate that Gpr85 influences the intrinsic electrophysiological properties of adult cerebellar GCs. Specifically, Gpr85-KO is associated with increased firing rates and higher membrane resistance, suggesting its involvement in the regulation of neuronal excitability.

Gpr85-KO larvae exhibit a stronger light-triggered startle response

We previously highlighted that Gpr85 is enriched at excitatory and inhibitory synapses in both the retina and the brain. We also reported that the receptor is expressed in key anatomical regions of the locomotor network and visual system, including the retina, optic tectum, cerebellum and spinal cord. Moreover, transcriptomic analyses of adult Gpr85-KO cerebellar GCs revealed gene expression changes related to neuronal activity and excitability. Finally, electrophysiological studies showed that Gpr85 deficiency alters the intrinsic neuronal properties of adult cerebellar GCs. Based on these findings, we hypothesized that Gpr85 could play a role in regulating neuronal activity within the locomotor and/or visual systems of zebrafish. To test this, we conducted behavioral experiments on Gpr85-KO larvae using the "Zebrabox" system to evaluate locomotor responses to dark/light stimuli.

Gpr85 heterozygous fish were incrossed, and their 6 dpf offspring were randomly and individually distributed into 48-well plates for analysis. We first recorded twenty minutes of activity in the dark to assess spontaneous locomotor activity under basal conditions (Fig. 6D). No significant differences in basal activity were observed between Gpr85-KO larvae and their siblings (*gpr85*$^{\Delta4/\Delta4}$ vs siblings$^{\Delta4}$, p = 0.36 and *gpr85*$^{GAL4/GAL4}$ vs siblings^{GAL4}, p = 0.94, M-W

test) (Fig. 6E). Next, we assessed the light-triggered startle response of Gpr85-KO larvae by measuring the distance swam during the first second following light onset (Fig. 6F). The experimental set up successfully detected the light-triggered startle response in control larvae, as evidenced by a significantly longer distance swam after light stimulation compared to the dark condition (siblings$^{\Delta 4}$: dark vs startle response, $p = 0.02$; siblings^{GAL4}: dark vs startle response, $p < 0.0001$, Wilcoxon test) (Fig. 6G, Movie 1). Compared to their siblings, both Gpr85-KO models displayed a more pronounced light-triggered startle response, as reflected by a modest yet significant increase in the distance swam following light induction (*gpr85*$^{\Delta 4/\Delta 4}$ mutants vs siblings$^{\Delta 4}$, $p = 0.015$; *gpr85*$^{GAL4/GAL4}$ mutants vs siblings^{GAL4}, $p = 0.011$, M-W test) (Fig. 6G). These results suggest that Gpr85 could be involved in the modulation of neuronal responses to light stimuli, potentially contributing to the regulation of visual and locomotor system activity.

Discussion

Although GPR85 was identified twenty-five years ago as one of the most well-conserved receptors in vertebrates, its biological functions remain elusive, and it continues to be classified as an orphan receptor. In this study, we significantly expanded our understanding of *gpr85* expression patterns across zebrafish development and adulthood. We provide the first evidence that Gpr85 is enriched at the plasma membrane of neuronal chemical synapses *in vivo* and demonstrate that constitutive Gpr85 deficiency alters the activity of adult zebrafish cerebellar GCs and light-induced motor behavior in larvae.

Using a newly generated *gpr85* reporter line combined with analyses of the “Daniocell” online resource, we documented neuronal *gpr85* expression throughout the zebrafish brain, spinal cord and retina development as observed in mice (Hellebrand *et al*, 2001). We also reported

gpr85 expression in developing neurons of the larval intestine, a novel finding. In adulthood, *gpr85* expression is maintained in the zebrafish brain and testes, consistent with observations in human (Matsumoto *et al*, 2000). We observed *gpr85* expression in brain regions also found in mammals, such as the olfactory bulb, dorsal pallium, subpallium, habenula (clusters of ventral *kiss1*$^{+}$ neurons present in right/left lobes), hypothalamus, cerebellum (granule cells in the granule cell layer, lobus caudalis and valvula cerebelli) and medulla oblongata. It was also found in the optic tectum and torus longitudinalis. The adult cerebellum exhibited high *gpr85* expression, consistent with observations made in mice (Regard *et al*, 2008). However, no expression was detected in Purkinje cells, in contrast to previous reports in the mouse model (Sakai *et al*, 2022). In line with human transcriptomic data (Lukowski *et al*, 2019; Yan *et al*, 2020), we identified *gpr85* expression in bipolar, amacrine and ganglion cells of the adult zebrafish retina. Additionally, as described in mice (Ito *et al*, 2009), we observed *gpr85* expression in neurons of the adult zebrafish intestinal myenteric plexus, and low-level expression was also detected in isolated epithelial cells of the villi, likely enteroendocrine cells, based on their distribution and elongated morphology (Gribble & Reimann, 2016).

At a subcellular level, we showed that Gpr85 is enriched in excitatory and inhibitory chemical synapses in both the developing and adult brain. This aligns with previous studies showing GPR85 binding to the postsynaptic marker PSD95 *in vitro* (Fujita-Jimbo *et al*, 2015) and its detection in isolated synaptosomes from the rat forebrain (Yoshimura *et al*, 2004). In the developing and adult retinal IPL, Gpr85 was also enriched at the plasma membrane of ribbon synapses, at both pre- and postsynaptic sites. This observation is consistent with our previous observation that GPR85 is targeted to the plasma membrane *in vitro* (Kaafarani *et al*, 2023). Interestingly, when detected on both sides of ribbon terminals, the receptor exhibited a reciprocal, clustered distribution, suggesting non-uniform localization within

synapses. While our observations are based on a tagged-Gpr85 overexpression model, future certification of these findings using a validated αGpr85 antibody would be valuable. Nevertheless, our approach underscores the receptor's enrichment at synaptic membranes of cerebral and retinal chemical synapses *in vivo*.

Unlike the sole documented GPR85-KO mouse model (Matsumoto *et al*, 2008; Chen *et al*, 2012), our zebrafish Gpr85-KO models exhibit no brain mass defects. Further investigations revealed that Gpr85 is dispensable for the developmental synaptogenesis of *gpr85*-expressing neurons' excitatory synaptic inputs, suggesting a non-essential role in nervous system development. To investigate the physiological changes induced by Gpr85 deficiency, we performed scRNAseq comparative transcriptomic analyses on sorted *gpr85*-expressing neurons from Gpr85-Ctl and KO brains. Cerebellar GCs were the predominant neuronal population in our dataset. We identified *oaz2b* as the most upregulated gene (FC = 5.13), alongside *oaz1b* also among the top upregulated genes (FC = 2.17), both encoding ornithine decarboxylase antizymes. These enzymes are key regulators of polyamine biosynthesis, as they inhibit ornithine decarboxylases, which are essential enzymes for polyamine synthesis (Pegg, 2009). Interestingly, previous studies have documented an increased intracellular polyamine levels and the upregulation of *OAZ1* and *OAZ2* in the brains of suicide completers (Guipponi *et al*, 2009; Sequeira *et al*, 2006; Chen *et al*, 2010; Fiori *et al*, 2011). This correlation suggests that the upregulation of *oaz* genes occurs in response to elevated polyamine concentrations. Conversely, the upregulation of these genes may lead to polyamine depletion. In both cases, regulation of *oaz* expression in the Gpr85-KO model unveils a potential link between Gpr85 and the polyamine system in the brain.

Another notable observation was the upregulation of several immediate early gene (IEG) orthologs (Lin *et al*, 2008; Okuno, 2011), including *npas4a*, *fosab* (c-fos ortholog), *egr1/4* and

junbb. In neurons such as GCs, these genes are known to be rapidly expressed in response to neuronal activity-induced intracellular Ca^{2+} changes (Monti *et al*, 2002; Contestabile *et al*, 2005). In our dataset, this upregulation was accompanied by increased expression of numerous genes functionally associated with neuronal firing activity and electrophysiological properties. These include genes involved in Ca^{2+}-dependent exocytosis (*synaptotagmins l5/14b/13/7b/2b/12*, *chromogranin a*, *synapsin 2b*, *Ca2⁺-dependent activator protein for secretion a*, *complexin 2)* and voltage-dependent ion channels (*chloride channel 2a*, *calcium channels alpha1b subunit/gamma subunit 8b* and *potassium channel subfamily H member 3*). Among neurotransmitter receptors, we observed an upregulation of the $GABA_A$ δ subunit (*gabrd*, FC = 2.4). Golgi and Purkinje cells exert tonic GABAergic inhibition on mammalian cerebellar GCs (Brickley *et al*, 1996; Hamann *et al*, 2002), primarily through extrasynaptic α6 $GABA_A$ receptors containing the δ subunit (Kaneda *et al*, 1995; Barnard *et al*, 1998; Brickley *et al*, 1999). Previous studies in the cerebellum have highlighted the role of tonic inhibition in regulating GCs excitability (Farrant & Nusser, 2005). In our context, *gabrd* upregulation may be a consequence of altered excitability associated with increased Gpr85-KO GCs activity. Altogether, our findings suggest that the absence of Gpr85 significantly alters the polyamine system and modifies cerebellar GC properties in favor of an increase in their electrophysiological activity.

Through *ex vivo* electrophysiological investigations of horizontal cerebellar slices using a cell-attached configuration, we confirmed that adult Gpr85-KO cerebellar GCs exhibited an increased spontaneous activity. To our knowledge, this study provides the first electrophysiological recordings of adult cerebellar GCs in zebrafish. Notably, while mammalian GCs are typically characterized by either no spontaneous activity *ex vivo* (D'Angelo, 2013) or a low firing rate *in vivo* (~0.5Hz) (Chadderton *et al*, 2004), we recorded

GCs with no (57%) or with a spontaneous activity in our controls (43%, 4.69 ± 1.24 Hz). Zebrafish cerebellar neuronal populations and the organization of the granule cell layer glomeruli are well conserved compared to mammals (Bae *et al*, 2009; Pose-Méndez *et al*, 2023). Glomerular synapses are both excitatory and inhibitory, mainly involving phasic glutamatergic and GABAergic transmission (D'Angelo, 2013). Given the thickness of our horizontal cerebellar slices (220 µm, approximately half the thickness of the adult zebrafish granule cell layer) and the absence of synaptic transmission blockage, the recorded activity is potentially influenced by residual inhibitory and/or excitatory synaptic transmission.

Consistent with the passive properties of rat cerebellar GCs (Chadderton *et al*, 2004), voltage-clamp assessments revealed that adult zebrafish cerebellar GCs exhibit a low membrane capacitance (2.46 ± 0.25 pF) and an average membrane time constant of 7.5 ± 0.93 ms. Further analysis revealed an increase in the membrane resistance (Rm) of Gpr85-KO GCs, while the membrane time constant and capacitance remained unaffected. This suggests fewer active and/or less abundant ion exchangers at the plasma membrane at -60mV. In our transcriptomic study, we observed upregulation of *ATPases* Na^+/K^+ pump subunits, including *ATPase* Na^+/K^+ *transporting subunit alpha 3b/1a.1* and *beta1b/2a*. These pumps play a major role in establishing the resting membrane potential (Pivovarov *et al*, 2018), suggesting that this upregulation likely represents a compensatory adaptation rather than a direct cause of the elevated Rm. While the mechanism by which Gpr85 affects Rm and the firing rate requires further investigation, our transcriptomic and electrophysiological findings suggest that Gpr85 modulates intrinsic properties and excitability of adult cerebellar GCs. Despite the recording of action potentials during whole-cell current-clamp protocols, the access resistance exceeded the standard limits, precluding reliable assessment of adult zebrafish GCs excitability *ex vivo*.

Studies from Matsumoto, Chen *et al.* (2008, 2012) documented behavioral changes in a spatial separation test and the Y-maze test in their mouse constitutive GPR85-deficient model. In the present work, we adapted a dark/light paradigm described by Campanari *et al.* (2020) and demonstrated that both Gpr85-KO models exhibit an increased response to light-induced aversive stimuli. Subtle yet consistent, this phenotype suggests that Gpr85 regulates light stimuli-induced behavioral responses. Based on our results, we hypothesize that Gpr85 influences neuronal circuit activity and, consequently, stimuli-induced behavioral responses, as it is expressed in several brain regions involved in visual and sensory-motor circuits. In line with this hypothesis, GPR85 knock-down and overexpression approaches have suggested that the receptor contributes to bone cancer pain in the rat spinal cord (Ni *et al*, 2023).

Although the precise mechanisms linking Gpr85 deficiency to the functional alteration of cerebellar GCs and behavioral changes of fish remain to be delineated, a number of potential links can be underlined with the sets of genes whose expression is modified in Gpr85-KO GCs. IEGs are well established markers of neuronal activity, including in GCs (Monti *et al*, 2002; Contestabile *et al*, 2005), and their upregulation likely reflects their increased excitability. As mentioned earlier, the upregulation of the *oaz* genes in Gpr85-KO GCs may lead to polyamine depletion. This latter is known to enhance NMDA receptor activity and alter AMPA and potassium channel functions, thereby increasing GC excitability (Makletsova *et al*, 2022).

Additionally, some of the observations might be linked to previous descriptions connecting the *GPR85* locus to ASD in humans (Fujita-Jimbo *et al*, 2015; Wu *et al*, 2022). ASD encompasses a range of neurodevelopmental diseases characterized by deficits in

communication and social interactions, as well as repetitive behaviors (Lord *et al*, 2018). There is mounting evidence pointing to a role of the cerebellum in cognition and emotion (Ma *et al*, 2023). Cerebellar GCs play key roles in motor coordination, cognitive processing and sensory integration (Rudolph *et al*, 2023), and their functional alteration, as observed in our Gpr85-KO fish, might lead to an imbalance of cerebello-cortical circuits leading to cognitive and social deficits observed in ASD.

In conclusion, our study shows that Gpr85 is localized at chemical synapses *in vivo*, and influences adult cerebellar granule cells electrophysiological activity as well as light-induced motor behavior in zebrafish larvae. These findings pave the way for future investigations into the molecular mechanisms through which Gpr85 modulates neuronal biology and sensory behaviors.

Material and methods

Zebrafish husbandry

Zebrafish were raised and maintained under standard laboratory conditions, in accordance with the Federation of European Laboratory Animal Science Associations (FELASA) guidelines (Aleström *et al*, 2020). All experimental procedures were approved by the Ethical Committee for Animal Welfare (CEBEA) of the Faculty of Medicine, Université Libre de Bruxelles. The zebrafish mutants and transgenic lines used in this study were *Tg(UAS:GFP-CAAX)*^{m1230} (Fernandes *et al*, 2012), *Tg(UAS:lifeact-eGFP)*^{mu271} (Helker *et al*, 2013) and *Tg(Xltubb:DsRed)*^{zf148} (Peri & Nüsslein-Volhard, 2008), here referred to as *Tg(NBT:DsRed)*. The term “adult” fish refers to animals aged between 6 and 8 months of age. For consistency and clarity throughout the text, transgenic animals are referenced without their allele designations.

Generation of *gpr85*$^{\Delta 4}$ knock-out and *gpr85*^{GAL4} knock-in mutants

Two sgRNAs were designed using Sequence Scan for CRISPR and CRISPR Scan software (http://crispr.dfci.harvard.edu/SSC/ (Xu *et al*, 2015) and http://www.cirsprscan.org/). The first *gpr85*-targeting sgRNA, used to generate the *gpr85*$^{\Delta 4}$ line, was synthetized *in vitro* as described previously (Talbot & Amacher, 2014), using the following targeting sequence: 5'-GGCGAACTACAGCCATGCAG -3'. *Gpr85*^{GAL4} mutants were generated using the Geneweld strategy, a variant of CRISPR/Cas9 technology for targeted integration (Wierson *et al*, 2020; Jordan M *et al*, 2021). The GAL4 coding sequence was inserted in frame with the endogenous *gpr85* start codon. We co-injected 0.5 nL of a solution containing Cas9 (100 ng/µL), the *gpr85*-targeting sgRNA2 (70 ng/µL, targeting sequence: 5'-AGTTCGCCATAGATGGAGAA-3'), UgRNA (40 ng/ µL) and the GAL4 donor vector (30 ng/µL) into *Tg(UAS:lifeact-eGFP)* one-cell stage embryos. According to the Geneweld approach, the GAL4 cargo was flanked by ugRNA-targeted sequences and the following 48 bp homology arms: left 5'-AGATCATGATCCTTGGCTAAAGCTTTAAGCGTTCTCTATGATCCCTTC-3', right 5'-TCCATCTATGGCGAACTACAGCCATGCAGGGGACCACAACATCTTACA-3'. F0 founders were screened at 3 dpf based on eGFP fluorescence. For both lines, individuals from at least the F3 generation were used in experiments. The following primers were used for genotyping and to validate the mutations by PCR and Sanger sequencing (Eurofins): *gpr85*-Forward 5′-GAGACAAAGGAACAAAGGATGC-3', *gpr85*-Reverse 5′-CAGGATGGATATCAGGAGGTTT-3', GAL4-Reverse 5′-TGCTGTCTCAATGTTAGAGGCATATC-3'.

Generation of transgenic lines

The following transgenes were randomly integrated into the genome of the *gpr85*^{GAL4} line: *Tg(zcUAS:FinGR(PSD95)-GFP-ZFC(CCR5TC)-KRAB(A))*, *Tg(ziUAS:FinGR(GPHN)-mCherry-ZFI(IL2RGTC)-KRAB(A))*, *Tg(UAS:zGpr85-eGFP), Tg(UAS:zGpr85-mCherry).* To achieve this, we co-injected 0.5 nL of a solution containing 120 ng/µL of *tol2* transposase mRNA and 40 ng/µL of the respective *tol2*-based vector into one-cell stage embryos. The *tol2*-UAS:zGpr85-eGFP vector was generated by digesting and ligating a *tol2*-UAS-MCS-EGFP plasmid (Genecust, Puc57 customed) with the amplified zebrafish *gpr85* coding sequence (zgpr85) using *Xho*I and *Bbv*CI restriction sites. The eGFP cassette of this newly generated vector was then replaced by an mCherry cassette using *Bbv*CI and *Sal*I restriction sites in order to generate the *tol2*-UAS:zGpr85-mCherry construct. The pTol2-zcUAS:PSD95.FinGR-GFP-ZFC(CCR5TC)-KRAB(A) and pTol2-ziUAS:GPHN.FinGR-mCherry-ZFI(IL2RGTC)-KRAB(A) plasmids were obtained from Joshua Bonkowsky's lab (Addgene plasmids #72638 and #72639, respectively). F0-injected embryos were screened and selected based on their GFP or mCherry fluorescence. Each F1 progeny derived from an F0 founder was screened for fluorescence and incrossed to establish stable F2 lines. For clarity, *Tg(zcUAS:FinGR(PSD95)-GFP-ZFC(CCR5TC)-KRAB(A))* and *Tg(FinGR(GPHN)-mCherry-ZFI(IL2RGTC)-KRAB(A))* lines are further referred to in the text as *Tg(UAS:FinGR(PSD)-GFP)* and *Tg(UAS:FinGR(GPHN)-mCherry)*, respectively.

WISH

Sense and antisense riboprobes for *gpr85* (ENSDARG00000068701) were synthesized *in vitro* using cDNA from 3 dpf embryos and the following primers: asFw 5'-TCAAAGACAAGAGCCTTCATCG-3', asRv 5'-GGATCCATTAACCCTCACTAAAGGGAACCTGCTTATCCGCTTTTCAGTT-3', sFw 5'-GGATCCATTAACCCTCACTAAAGGGAATCAAAGACAAGAGCCTTCATCG-3', sRv 5'-

CCTGCTTATCCGCTTTTCAGTT-3'. Forward primers contain the T3 polymerase promoter sequence. WISH was performed using a standard protocol (Thisse & Thisse, 2008). To ensure specificity of the staining, the sense and antisense riboprobes were always hybridized in parallel. Probe hybridization was carried out at 65°C and BM-purple (Roche) was used as the substrate for signal revelation.

Gene expression analysis by qPCR

For each biological replicate, 30 larvae were digested in TRIzol reagent (Qiagen). RNA was isolated by chloroform extraction and purified with the RNAeasy Mini Kit (Qiagen). Genomic DNA contamination was removed using the TURBO DNA-*free*™ kit (Thermo Fisher Scientific). The cDNAs were prepared from 2 µg of purified RNA using Super Script II reverse transcriptase with Oligo(dT) primers (Thermo Fisher Scientific). qPCRs were performed using the CFX96™ Real-Time System (Bio-rad, CA) according to the manufacturer's instructions. Biological replicates were tested in duplicate, and relative transcript levels were assessed using the ΔC_T method. Gene expression levels were normalized to two reference genes (*rpl13* and *lms12b*). The following primers were used: *gpr85* Forward 5′-GCATCTTCTCCAACCGAGAG-3', Reverse 5′-AAAACAAACGCCACAGAACC-3'; *rpl13* Forward 5′-TCTGGAGGACTGTAAGAGGTATGC-3', Reverse 5′-AGACGCACAATCTTGAGAGCAG-3'; *lms12b* Forward 5′-AGCCATGTCTCTTGCCTCAC-3', Reverse 5′-ATGACGTCACTGAGGTTGGG-3'.

Fluorescent immunostaining

Embryos and larvae were fixed overnight in 4% PFA and processed for either whole-mount or cryosection antibody staining. Adult organs were dissected and fixed in 4% PFA at 4°c for 4 hours, then incubated for over 2 days at 4°c in 30% sucrose. The samples were then

embedded in OCT, snap-frozen and cryosectioned (14 µm, Leica CM3050 S). Staining procedures were performed according to previously described protocols (whole-mount: Ferrero *et al*, 2018; cryosections: Ferrero *et al*, 2020). The following antibodies were used: chicken anti-GFP polyclonal (ab13970, Abcam, 1:1000), mouse anti-mCherry monoclonal (632543, Takara, 1:1000), mouse anti-HuC/D monoclonal (A-21271, Invitrogen, 1:250), mouse anti-PCNA monoclonal (M0879, Dako, 1:250), rabbit anti-DsRed polyclonal (632496, Takara, 1:1000), rabbit anti-Ribeye-A polyclonal (s4561-2, Zenisek lab, 1:1000), goat Alexa Fluor 488-conjugated anti-chicken IgG antibody (ab150169, Abcam, 1:500), donkey Alexa Fluor 594-conjugated anti-rabbit IgG (ab150076, Abcam, 1:500) and donkey Alexa Fluor 594-conjugated anti-mouse IgG (ab150108, Abcam; 1:500).

Zebrafish morphometric measurements

Gpr85^{GAL4} and *Gpr85*$^{\Delta 4}$ heterozygous mutants were respectively incrossed and their corresponding adult offspring were analyzed. The body length was measured using a ruler. The brain was dissected, carefully dried using absorbent paper, and weighted using a precision balance (Sartorius Entris II, BCE224I-1S). Brains with dissection defects were discarded. All measurements were performed before genotyping.

Tissue clearing

For adult brain tissue clearing, a modified EZ Clearing method (Hsu *et al*, 2022) was used. Zebrafish heads were dissected and enucleated, followed by overnight fixation in 4% PFA (pH 8.5) at 4°C. All subsequent steps were performed under agitation at 4°C. Whole fixed brains were dissected and incubated overnight in 50% (v/v) THF (Sigma-Aldrich, 186562) in sterile Milli-Q water (pH adjusted to 8.5 with triethylamine, Sigma-Aldrich, T0886). Samples were then washed four times (1h each) with sterile Milli-Q water. Finally, samples were

submerged in refractive index (RI) matching EZ View solution (80% Nycodenz, Accurate Chemical & Scientific AN1002423, 7 M Urea, 0.05% sodium azide in 0.02 M sodium phosphate buffer; prepared according to Hsu *et al*, 2022) and stored at 4ºC for at least 24h before imaging.

Electron microscopy

Structural analysis

Wild-type (WT) and *gpr85*$^{\Delta 4/\Delta 4}$ larvae were fixed for 4 days at 4°C in 2.5% glutaraldehyde. Unless specified, all subsequent steps were performed at room temperature. The samples were rinsed in 0.1 M cacodylate buffer, pH 7.4, then stained for 1 h in 1% osmium tetroxide-1.5% ferrocyanide (0.1 M cacodylate), 1 h in 1% osmium tetroxide (0.1 M cacodylate), followed by 1.5 h in 1% uranyl acetate (ultrapure water). The larvae were next embedded in 1% agarose and underwent dehydration in graded ethanol solutions (50%, 70%, 95% and 100%). Ethanol was then replaced with 100% propylene oxide (PO, two successive 8-min baths), then with a 50/50 mixture of PO/epoxy resin (Agar scientific, Agar 100) for 1 h, and with 100% epoxy resin for 3 h. The resin was finally changed and polymerized for 2 days at 60°C.The resulting blocks were sectioned using a UC7 ultramicrotome (LEICA EM) and collected on carbon-formvar 100 mesh copper grids (EMS).

Immunogold staining

Gpr85$^{GAL4/+}$; *Tg(UAS:zgpr85-mCherry)* larvae were fixed for 2 weeks at 4°C in 4% PFA-0.5% glutaraldehyde, then embedded in 12% gelatin blocks (in ultrapure water). Unless specified, the following steps were performed at room temperature. Microdissection was performed to retain only the head of the zebrafish. The obtained blocks were incubated for 2 days in 2.3 M sucrose on a rotating wheel at 4°C, then stored at 4°C before processing. Next, the blocks

were mounted on supports and sectioned using a UC6 ultramicrotome equipped with an FC6 cryo-chamber (LEICA EM). Sections were made at -120°C and placed on carbon-formvar 100 mesh nickel grids (EMS). The grids were processed for immunogold labeling as follows. Samples were blocked for 30 minutes in 5% goat serum and incubated O/N at 4°C with the following primary antibodies: rabbit anti-DsRed polyclonal (632496, Takara, 1:50) or rabbit polyclonal anti-Ribeye-A (s4561-2, Zenisek lab, 1:50) in 3% goat serum. The grids were washed in TBS buffer, then incubated with a secondary anti-rabbit antibody (1:100, Sigma-Aldrich) for 1h at 37°C in TBS. The grids were washed in TBS buffer, followed by washes in ultrapure water. Finally, the grids were stained for 10 minutes on ice with methylcellulose-4% uranyl acetate (9:1). The grids were observed using a Tecnai 10 100kV transmission electron microscope (FEI, Thermo Fisher Sci). Images were captured with a MegaView 14 bits camera (Olympus) and processed using the iTEM software (Olympus).

Light microscopy imaging and image analysis

WISH and live embryos/larvae were imaged using a Leica M165FC fluorescent stereomicroscope equipped with a Leica DFC7000T digital camera. Images were acquired using the LAS software (Leica, V4.6.2). Immunostained whole-mount larvae and cryosections were imaged using a Zeiss LSM 780 inverted confocal microscope, with Plan Apochromat 20x/0.8 M27, LD C Apochromat 40x/1.1 W korr M27 and Plan achromat 63x/1.46 oil Korr M27 objectives. Quantification of GFP^+ neuronal soma within the optic tectum stratum paraventriculare was performed using ImageJ software. The area of individual hemisphere used for the quantification was drawn manually and the entire sections were analyzed (z-stacks, 3 µm steps). Quantification of FinGR(PSD)-GFP^+ puncta density in the optic tectal neuropils was performed using Imaris software. Puncta detection was based on an estimated diameter of 0.3 µm with background subtraction applied. Two identical rectangular soma-free

areas (1616 μm^2 each) per optic section were defined for quantification. Three optic sections per hemisphere per larva were measured and averaged. Cleared brain samples were sagitally cut between the hemispheres and immersed cut-face down in a RI matching solution. Images were acquired with a Nikon AX/R confocal microscope system using a 10X/0.45 Plan Apo LambdaD objective lens in resonant scanning mode. Acquisition settings were adjusted to 1.3-1.8X zoom with 2048x2048 pixel resolution and a tile scan setting with 5% overlap. Online stitching mode was enabled in for real-time stitching during acquisition. Images were post-processed with 3D Deconvolution, and with Denoise.ai, in NIS-Elements AR software to obtain sharper Z-resolution.

Comparative scRNAseq and data analysis

scRNAseq library preparation and sequencing

Adult brains from siblings (one control and one *gpr85*-KO) were dissected and digested with 14 U papain (Sigma-Aldrich, p4762) at 33°C for 10 to 15 minutes in 0.9X Dulbecco's Phosphate Buffered Saline (DPBS). Mechanical dissociation was performed during this process using a syringe with a 26 G needle (B.Braun, Omnifix 100 Duo). Cell suspensions were washed and centrifuged (300 g) in 2% fetal bovine serum diluted in 0.9X DPBS (FACS buffer). Then, cells were resuspended in FACS buffer and filtered using a sterile 40 µm nylon mesh (VWR). Cell sorting of $eGFP^+$ cells was performed on a FACS ARIA (Becton Dickinson, San Jose, CA) using Sytox Red (5 nM, Thermofisher scientific S34859) in order to remove dead cells. 50,000 cells were sorted per condition with an expected final density of 294 cells/µL. The library was prepared following 10x Genomics Chromium Single cell 3’ kit (v3) guidelines and the libraries were sequenced using an Illumina NovaSeq 6000.

scRNAseq data processing

Raw sequencing data were processed using Cell Ranger (v7.1.0) with a custom-built reference based on the zebrafish reference genome GRCz11 and gene annotation Ensembl 92 in which the GFP sequence was added. Data were analyzed through the Seurat Package in R (Stuart *et al*, 2019), keeping only cells having between 500 to 10,000 counts with less than 7.5% of genes coming from the mitochondrial genome. SCTransform was used as the scaling method (Hafemeister & Satija, 2019). The UMAPs were generated using 10 dimensions with a clustering resolution of 0.5.

Electrophysiology

Adult brains from *gpr85*$^{GAL4/+}$ (or *gpr85*$^{GAL4/GAL4}$), *Tg(UAS:Lifeact-eGFP)* individuals were dissected, and *ex vivo* horizontal cerebellar slices (220 µm thick) were produced using a Vibratome R VT 1000 S (Leica, Wetzlar, Germany) in an ice-cold solution (2.5 mM KCl, 1.25 mM NaH_2PO_4, 25 mM $NaHCO_3$, 7 mM $MgCl_2$, 0.5 mM $CaCl_2$, 14 mM glucose, and 139 mM choline chloride) gassed with a carbogen solution (95% O_2 and 5% CO_2). Then, slices were transferred to the recovery chamber at 26°C and incubated in artificial cerebrospinal fluid (aCSF) containing: 127 mM NaCl, 2.5 mM KCl, 1.25 mM NaH_2PO_4, 1 mM $MgCl_2$, 26 mM $NaHCO_3$, 10 mM D-glucose, 2 mM $CaCl_2$, bubbled with a mixture of 95% O_2 and 5% CO_2 at a pH of 7.3 (300-316 mOsm). After a recovery period of 45 min, individual slices were transferred to the recording chamber continuously superfused with aCSF at a rate of 1-1.5 ml/min at room temperature (24-26°C). Cerebellar GCs were identified with a 63x water immersion objective from a Zeiss Axioskop microscope (Axioskop 2FS Plus; 140 Zeiss, Oberkochen, Germany) equipped with an infrared CCD camera (XST70CE, Hamamatsu Photonics KK, Hamamatsu, Japan). GCs were selected based on their eGFP expression using the filter set 38 HE (BP: 470/40 wavelength, Carl Zeiss Instruments, Oberkochen, Germany) and the OptoLED R electroluminescent diode (Cairn Research Lda, Kent,

England). Borosilicate-glass patch electrodes (Hilgenberg GmbH, Malsfeld, Germany) (resistance between 5 and 7 MΩ) filled with 125 mM $KMeSO_3$, 12 mM KCl, 0.022 mM $CaCl_2$, 4 mM $MgCl_2$, 10 mM HEPES, 0.1 mM EGTA, 5 mM Na_2-phosphocreatine, 4 mM Mg_2-ATP and 0.5 mM Na_2-GTP, were used for the recordings. Cerebellar GCs were first recorded in cell-attached and then in whole-cell configurations to examine their intrinsic properties. Recordings were performed using an EPC-10 patch clamp amplifier (HEKA, Lambrecht, Germany) and PatchMaster acquisition software (HEKA). Signals were sampled at 20 kHz with a gain of 2 mV/pA and lowpass filtered at 2.9 kHz.

Extracellular spontaneous action potentials were acquired in cell-attached configuration (Seal > 1 GΩ, 60 to 120 s recordings). Standard off-line detection of action potential was performed with Axograph X software (Axon Instruments Inc., Foster City, CA). For this analysis, we generated an action potential template to scan the recording trace. All matching events were stored, and false positive events were detected and discarded based on their amplitude. Spontaneous firing frequencies were assessed with 60 second recordings. Cells were then recorded in whole-cell configuration in voltage-clamp mode at holding potential of -60 mV. Passive membrane properties and access resistance were extracted from current traces, averaged on ten sweeps recorded in response to a hyperpolarizing voltage pulse (200 ms) of 10 mV from holding potential. The membrane resistance was computed using the difference between the baseline current and the current at 20 ms during the voltage step. The integrated area under the transient was used to determine membrane capacitance. Membrane time constant was calculated as the product of the Rm multiplied by the Cm. If access resistance changed more than 25% between the beginning and the end of the recording, the neuron was excluded from the analysis. All analysis were performed using IgorPro 6.3 software (WaveMetrics, Portland, USA) using Patcher's Power Tools, NeuroMatic plugins and Microsoft Excel software were used.

Behavioral experiments

Larvae were randomly assigned and individually immerged in 1 mL of E3 standard medium (5 mM NaCl, 0.17 mM KCl, 0.33 mM $CaCl_2$, 0.33 mM $MgSO_4$, dH_2O) (Fetcho, 2003) in 48 well-plates (VWR) and placed in a standard Zebrabox (Viewpoint) for recording. Larvae presenting developmental defects such as trunk curvature and/or pericardial edema were excluded from the experiments. The temperature of the chamber was maintained at 28°c and all recordings were performed after a 5-min habituation step in the dark. Experimental set up and data were generated using Viewpoint's Zebralab software. The spontaneous locomotor activity in the dark was assessed over a 20-min integration period while the light-triggered startle response was induced using 100% light intensity (8000 lx) and measured over a 1-second integration period.

Statistical Analysis

Statistical analyses were conducted using Graphpad Prism8. Student's t-test or Mann Whitney U test was applied depending on the dataset. Normality was assessed using the D'Agostino-Pearson omnibus normality test. Wilcoxon matched-pairs rank test was used to compare basal locomotor activity in the dark versus light-induced startle response for a given condition. The results are considered significant when $p < 0.05$ and are displayed with the mean and standard error of the mean (SEM) or the standard deviation (SD, Fig. 6E,G). Sample sizes and quantification methods are specified in the respective figure legends.

DATA availability

The datasets produced in this study are available at GSE291414.

Acknowledgements

We are grateful to Sumeet Pal Singh, Elif Sema Eski, and Gilles Dinsart for their assistance with single-cell data processing. We thank Jean-Marie Vanderwinden and Michiel Martens from the ULB Limif Platform, as well as Christine Dubois from the FACS facility. We thank Courtney Elaine Frederick and David Zenisek for generously donating an aliquot of their αRibeye antibody. We thank Jeffrey Farrel and Abhinav Sur for their permission to use "Daniocell's" website images. We also thank Eva Laurrel and the other members of the zebrafish "mapzebrain" atlas project. Finally, we thank Mustapha Chaouni and Kamel Gharbi for their daily maintenance of the fishroom facility. This project was funded by the "Fonds David et Alice Van Buuren" and the Fonds National de la Recherche Scientifique (FNRS: CDR J021.517F and FRIA fellowship).

Conflict of interest statement

All authors declare no conflict of interest.

Author contributions

Romain Darche-Gabinaud: Conceptualization; Data curation; Formal analysis; Funding acquisition; Investigation; Visualization; Methodology; Writing—original draft; Writing—review and editing.

Abeer Kaafarani: Conceptualization; Molecular biology; Review and editing.

Marine Chazalon: Resources; Data curation; Formal analysis; Investigation.

Valérie Suain: Resources; Data curation; Formal analysis; Investigation; Visualization; Methodology.

Erika Hendrick: Resources; Data curation; Formal analysis; Investigation; Visualization; Methodology.

Louise Conrard: Resources; Data curation; Formal analysis; Investigation; Visualization; Methodology.

Anne Lefort: Resources; Formal analysis; Methodology.

Frédérick Libert: Resources; Software; Formal analysis; Methodology.

Mehmet Can Demirler: Resources; Visualization; Methodology.

Serge Schiffmann: Conceptualization; Resources; Data curation; Supervision; Writing—Review and editing.

David Perez-Morga: Conceptualization; Resources; Data curation; Supervision.

Valérie Wittamer: Conceptualization; Resources; Data curation; Software; Formal analysis; Supervision; Funding acquisition; Validation; Investigation; Visualization; Methodology; Project administration.

Isabelle Pirson: Conceptualization; Resources; Data curation; Software; Formal analysis; Supervision; Funding acquisition; Validation; Investigation; Visualization; Methodology; Writing—original draft; Project administration; Writing—review and editing.

Marc Parmentier: Conceptualization; Resources; Data curation; Software; Formal analysis; Supervision; Funding acquisition; Validation; Investigation; Visualization; Methodology; Writing—original draft; Project administration; Writing—review and editing.

References

Aleström P, D'Angelo L, Midtlyng PJ, Schorderet DF, Schulte-Merker S, Sohm F & Warner S (2020) Zebrafish: Housing and husbandry recommendations. *Lab Anim* 54: 213–224

Bae Y-K, Kani S, Shimizu T, Tanabe K, Nojima H, Kimura Y, Higashijima S & Hibi M (2009) Anatomy of zebrafish cerebellum and screen for mutations affecting its development. *Dev Biol* 330: 406–426

Barnard EA, Skolnick P, Olsen RW, Mohler H, Sieghart W, Biggio G, Braestrup C, Bateson AN & Langer SZ (1998) International Union of Pharmacology. XV. Subtypes of gamma-aminobutyric acidA receptors: classification on the basis of subunit structure and receptor function. *Pharmacol Rev* 50: 291–313

Breton TS, Fike S, Francis M, Patnaude M, Murray CA & DiMaggio MA (2023) Characterizing the SREB G protein-coupled receptor family in fish: Brain gene expression and genomic differences in upstream transcription factor binding sites. *Comp Biochem Physiol A Mol Integr Physiol* 285: 111507

Brickley SG, Cull-Candy SG & Farrant M (1996) Development of a tonic form of synaptic inhibition in rat cerebellar granule cells resulting from persistent activation of GABAA receptors. *J Physiol* 497: 753

Brickley SG, Cull-Candy SG & Farrant M (1999) Single-channel properties of synaptic and extrasynaptic GABAA receptors suggest differential targeting of receptor subtypes. *J Neurosci Off J Soc Neurosci* 19: 2960–2973

Campanari M-L, Bourefis A-R, Buee-Scherrer V & Kabashi E (2020) Freezing activity brief data from a new FUS mutant zebrafish line. *Data Brief* 31: 105921

Chadderton P, Margrie TW & Häusser M (2004) Integration of quanta in cerebellar granule cells during sensory processing. *Nature* 428: 856–860

Chen Q, Kogan JH, Gross AK, Zhou Y, Walton NM, Shin R, Heusner CL, Miyake S, Tajinda K, Tamura K, *et al* (2012) SREB2/GPR85, a schizophrenia risk factor, negatively regulates hippocampal adult neurogenesis and neurogenesis-dependent learning and memory. *Eur J Neurosci* 36: 2597–2608

Contestabile A, Fila T, Bartesaghi R & Ciani E (2005a) Cyclic AMP-mediated Regulation of Transcription Factor Lot1 Expression in Cerebellar Granule Cells*. *J Biol Chem* 280: 33541–33551

Contestabile A, Fila T, Bartesaghi R & Ciani E (2005b) Cyclic AMP-mediated regulation of transcription factor Lot1 expression in cerebellar granule cells. *J Biol Chem* 280: 33541–33551

D'Angelo E (2013) Cerebellar Granule Cell. In *Handbook of the Cerebellum and Cerebellar Disorders*, Manto M Schmahmann JD Rossi F Gruol DL & Koibuchi N (eds) pp 765–791. Dordrecht: Springer Netherlands

Farrant M & Nusser Z (2005) Variations on an inhibitory theme: phasic and tonic activation of GABA(A) receptors. *Nat Rev Neurosci* 6: 215–229

Ferrero G, Gomez E, lyer S, Rovira M, Miserocchi M, Langenau DM, Bertrand JY & Wittamer V (2020) The macrophage-expressed gene (mpeg) 1 identifies a subpopulation of B cells in the adult zebrafish. *J Leukoc Biol* 107: 431–443

Ferrero G, Mahony CB, Dupuis E, Yvernogeau L, Di Ruggiero E, Miserocchi M, Caron M, Robin C, Traver D, Bertrand JY, *et al* (2018) Embryonic Microglia Derive from Primitive Macrophages and Are Replaced by *cmyb*-Dependent Definitive Microglia in Zebrafish. *Cell Rep* 24: 130–141

Fetcho J (2003) Zebrafish: A Practical Approach. The Practical Approach Series, Volume 261. Edited by Christiane Nüsslein-Volhard and Ralf Dahm. *Q Rev Biol* 78: 477–478

Fiori LM, Bureau A, Labbe A, Croteau J, Noël S, Mérette C & Turecki G (2011) Global gene expression profiling of the polyamine system in suicide completers. *Int J Neuropsychopharmacol* 14: 595–605

Fujita-Jimbo E, Tanabe Y, Yu Z, Kojima K, Mori M, Li H, Iwamoto S, Yamagata T, Momoi MY & Momoi T (2015) The association of GPR85 with PSD-95-neuroligin complex and autism spectrum disorder: a molecular analysis. *Mol Autism* 6: 17

Gribble FM & Reimann F (2016) Enteroendocrine Cells: Chemosensors in the Intestinal Epithelium. *Annu Rev Physiol* 78: 277–299

Hafemeister C & Satija R (2019) Normalization and variance stabilization of single-cell RNA-seq data using regularized negative binomial regression. *Genome Biol* 20: 296

Hamann M, Rossi DJ & Attwell D (2002) Tonic and Spillover Inhibition of Granule Cells Control Information Flow through Cerebellar Cortex. *Neuron* 33: 625–633

Helker CSM, Schuermann A, Karpanen T, Zeuschner D, Belting H-G, Affolter M, Schulte-Merker S & Herzog W (2013) The zebrafish common cardinal veins develop by a novel mechanism: lumen ensheathment. *Dev Camb Engl* 140: 2776–2786

Hellebrand S, Schaller HC & Wittenberger T (2000) The brain-specific G-protein coupled receptor GPR85 with identical protein sequence in man and mouse maps to human chromosome 7q311. *Biochim Biophys Acta BBA - Gene Struct Expr* 1493: 269–272

Hellebrand S, Wittenberger T, Schaller HC & Hermans-Borgmeyer I (2001) Gpr85, a novel member of the G-protein coupled receptor family, prominently expressed in the developing mouse cerebral cortex. *Brain Res Gene Expr Patterns* 1: 13–16

Hsu C-W, Cerda J III, Kirk JM, Turner WD, Rasmussen TL, Flores Suarez CP, Dickinson ME & Wythe JD (2022) EZ Clear for simple, rapid, and robust mouse whole organ clearing. *eLife* 11: e77419

Ito J, Ito M, Nambu H, Fujikawa T, Tanaka K, Iwaasa H & Tokita S (2009) Anatomical and histological profiling of orphan G-protein-coupled receptor expression in gastrointestinal tract of C57BL/6J mice. *Cell Tissue Res* 338: 257–269

Jeon J, Kim C, Sun W, Chung H, Park S-H & Kim H (2002) Cloning and localization of rgpr85 encoding rat G-protein-coupled receptor. *Biochem Biophys Res Commun* 298: 613–618

Jin C, Kang H, Kim S, Zhang Y, Lee Y, Kim Y & Han K (2018a) Transcriptome analysis of Shank3-overexpressing mice reveals unique molecular changes in the hypothalamus. *Mol Brain* 11: 71

Jin C, Kang H, Ryu JR, Kim S, Zhang Y, Lee Y, Kim Y & Han K (2018b) Integrative Brain Transcriptome Analysis Reveals Region-Specific and Broad Molecular Changes in Shank3-Overexpressing Mice. *Front Mol Neurosci* 11: 250

Jordan M W, Wa W, Mp A, Cm M, Me T, Z M, Sc E, Kj C, Dl D, Jj E, *et al* (2021) GeneWeld: Efficient Targeted Integration Directed by Short Homology in Zebrafish. *Bio-Protoc* 11

Kaafarani A, Darche-Gabinaud R, Bisteau X, Imbault V, Wittamer V, Parmentier M & Pirson I (2023) Proximity Interactome Analysis of Super Conserved Receptors Expressed in the Brain Identifies EPB41L2, SLC3A2, and LRBA as Main Partners. *Cells* 12: 2625

Kaneda M, Farrant M & Cull-Candy SG (1995) Whole-cell and single-channel currents activated by GABA and glycine in granule cells of the rat cerebellum. *J Physiol* 485 (Pt 2): 419–435

Kim C-H, Ueshima E, Muraoka O, Tanaka H, Yeo S-Y, Huh T-L & Miki N (1996) Zebrafish *elav*/HuC homologue as a very early neuronal marker. *Neurosci Lett* 216: 109–112

Kress S & Wullimann MF (2012) Correlated basal expression of immediate early gene egr1 and tyrosine hydroxylase in zebrafish brain and downregulation in olfactory bulb after transitory olfactory deprivation. *J Chem Neuroanat* 46: 51–66

Kühn E & Köster RW (2010) Analysis of gene expression by in situ hybridization on adult zebrafish brain sections. *Cold Spring Harb Protoc* 2010: pdb.prot5382

Lin Y, Bloodgood BL, Hauser JL, Lapan AD, Koon AC, Kim T-K, Hu LS, Malik AN & Greenberg ME (2008) Activity-dependent regulation of inhibitory synapse development by Npas4. *Nature* 455: 1198–1204

Lord C, Elsabbagh M, Baird G & Veenstra-Vanderweele J (2018) Autism spectrum disorder. *The Lancet* 392: 508–520

Lukowski SW, Lo CY, Sharov AA, Nguyen Q, Fang L, Hung SS, Zhu L, Zhang T, Grünert U, Nguyen T, *et al* (2019) A single-cell transcriptome atlas of the adult human retina. *EMBO J* 38: e100811

Ma Q, Baetens K, Crunelle CL & Heleven E (2023) Editorial: A multi-talented butterfly: the role of the cerebellum in social cognition, emotion, and language. *Front Hum Neurosci* 17: 1322977

Makletsova MG, Rikhireva GT, Kirichenko EYu, Trinitatsky IYu, Vakulenko MYu & Ermakov AM (2022) The Role of Polyamines in the Mechanisms of Cognitive Impairment. *Neurochem J* 16: 283–294

Matsumoto M, Beltaifa S, Weickert CS, Herman MM, Hyde TM, Saunders RC, Lipska BK, Weinberger DR & Kleinman JE (2005) A conserved mRNA expression profile of SREB2 (GPR85) in adult human, monkey, and rat forebrain. *Brain Res Mol Brain Res* 138: 58–69

Matsumoto M, Saito T, Takasaki J, Kamohara M, Sugimoto T, Kobayashi M, Tadokoro M, Matsumoto S, Ohishi T & Furuichi K (2000) An Evolutionarily Conserved G-Protein Coupled Receptor Family, SREB, Expressed in the Central Nervous System. *Biochem Biophys Res Commun* 272: 576–582

Matsumoto M, Straub RE, Marenco S, Nicodemus KK, Matsumoto S-I, Fujikawa A, Miyoshi S, Shobo M, Takahashi S, Yarimizu J, *et al* (2008) The evolutionarily conserved G protein-coupled receptor SREB2/GPR85 influences brain size, behavior, and vulnerability to schizophrenia. *Proc Natl Acad Sci U S A* 105: 6133–6138

Monti B, Marri L & Contestabile A (2002) NMDA receptor-dependent CREB activation in survival of cerebellar granule cells during in vivo and in vitro development. *Eur J Neurosci* 16: 1490–1498

Ni H, Xu M, Kuang J, Xu C, He Q, Luo G, Fu J, Zhu J, Ni C, Zhao B, *et al* (2023) Upregulation of LncRNA71132 in the spinal cord regulates hypersensitivity in a rat model of bone cancer pain. *Pain* 164: 180–196

Okuno H (2011) Regulation and function of immediate-early genes in the brain: Beyond neuronal activity markers. *Neurosci Res* 69: 175–186

Park H-C, Kim C-H, Bae Y-K, Yeo S-Y, Kim S-H, Hong S-K, Shin J, Yoo K-W, Hibi M, Hirano T, *et al* (2000) Analysis of Upstream Elements in the *Hu*C Promoter Leads to the Establishment of Transgenic Zebrafish with Fluorescent Neurons. *Dev Biol* 227: 279–293

Pegg AE (2009) Mammalian polyamine metabolism and function. *IUBMB Life* 61: 880–894

Peri F & Nüsslein-Volhard C (2008) Live Imaging of Neuronal Degradation by Microglia Reveals a Role for v0-ATPase a1 in Phagosomal Fusion In Vivo. *Cell* 133: 916–927

Pivovarov AS, Calahorro F & Walker RJ (2018) Na+/K+-pump and neurotransmitter membrane receptors. *Invert Neurosci* 19: 1

Pose-Méndez S, Schramm P, Valishetti K & Köster RW (2023) Development, circuitry, and function of the zebrafish cerebellum. *Cell Mol Life Sci* 80: 227

Rudolph S, Badura A, Lutzu S, Pathak SS, Thieme A, Verpeut JL, Wagner MJ, Yang Y-M & Fioravante D (2023) Cognitive-Affective Functions of the Cerebellum. *J Neurosci* 43: 7554–7564

Sakai A, Yasui T, Watanave M, Tatsumi R, Yamamoto Y, Takano W, Tani Y, Okamura I, Hirai H & Takeda S (2022) Development of novel potent ligands for GPR85, an orphan G protein-coupled receptor expressed in the brain. *Genes Cells* 27: 345–355

Shainer I, Kuehn E, Laurell E, Al Kassar M, Mokayes N, Sherman S, Larsch J, Kunst M & Baier H (2023) A single-cell resolution gene expression atlas of the larval zebrafish brain. *Sci Adv* 9: eade9909

Shainer I, Kuehn E, Laurell E, Al Kassar M, Mokayes N, Sherman S, Larsch J, Kunst M & Baier H (2023) (https://daniocell.nichd.nih.gov/gene/G/gpr85/gpr85.html) [DATASET]

Son J-H, Keefe MD, Stevenson TJ, Barrios JP, Anjewierden S, Newton JB, Douglass AD & Bonkowsky JL (2016) Transgenic FingRs for Live Mapping of Synaptic Dynamics in Genetically-Defined Neurons. *Sci Rep* 6: 18734

Stuart T, Butler A, Hoffman P, Hafemeister C, Papalexi E, Mauck WM, Hao Y, Stoeckius M, Smibert P & Satija R (2019) Comprehensive Integration of Single-Cell Data. *Cell* 177: 1888-1902.e21

Sur A, Wang Y, Capar P, Margolin G, Prochaska MK & Farrell JA (2023) Single-cell analysis of shared signatures and transcriptional diversity during zebrafish development. *Dev Cell* 58: 3028-3047.e12

Sur A, Wang Y, Capar P, Margolin G, Prochaska MK & Farrell JA (2023) (https://daniocell.nichd.nih.gov/) [DATASET]

Talbot JC & Amacher SL (2014) A streamlined CRISPR pipeline to reliably generate zebrafish frameshifting alleles. *Zebrafish* 11: 583–585

Thisse B & Thisse C (2004) Fast Release Clones: A High Throughput Expression Analysis. ZFIN Direct Data Submission. (http://zfin.org)

Thisse C & Thisse B (2008) High-resolution in situ hybridization to whole-mount zebrafish embryos. *Nat Protoc* 3: 59–69

Wierson WA, Welker JM, Almeida MP, Mann CM, Webster DA, Torrie ME, Weiss TJ, Kambakam S, Vollbrecht MK, Lan M, *et al* (2020) Efficient targeted integration directed by short homology in zebrafish and mammalian cells. *eLife* 9: e53968

Wu X, Yang H, Lin H, Suo A, Wu S, Xie W, Zhou N, Guo S, Ding H, Zhou G, *et al* (2022) Characterizing microRNA editing and mutation sites in Autism Spectrum Disorder. *Front Mol Neurosci* 15: 1105278

Xu H, Xiao T, Chen C-H, Li W, Meyer CA, Wu Q, Wu D, Cong L, Zhang F, Liu JS, *et al* (2015) Sequence determinants of improved CRISPR sgRNA design. *Genome Res* 25: 1147–1157

Yan W, Peng Y-R, van Zyl T, Regev A, Shekhar K, Juric D & Sanes JR (2020) Cell Atlas of The Human Fovea and Peripheral Retina. *Sci Rep* 10: 9802

Yoshimura Y, Yamauchi Y, Shinkawa T, Taoka M, Donai H, Takahashi N, Isobe T & Yamauchi T (2004) Molecular constituents of the postsynaptic density fraction revealed by proteomic analysis using multidimensional liquid chromatography-tandem mass spectrometry. *J Neurochem* 88: 759–768

Figures Legends

Figure 1. Gpr85 is broadly expressed by maturing neurons in the zebrafish brain parenchyma during late embryogenesis.

A-E Lateral views of live *gpr85*$^{GAL4/+}$, *Tg(UAS:GFP-CAAX)* zebrafish embryos at 1dpf with brightfield (A) and fluorescence imaging (B-E) showing the GFP-CAAX signal in the brain and spinal cord at 1 dpf (B), 2 dpf (C), 3 dpf (D), and 6 dpf (E). Scale bars: 50 µm.

F-I''' Maximum projection confocal images of coronal sections of the brain from a 3 dpf *gpr85*$^{GAL4/+}$, *Tg(UAS:Lifeact-eGFP)* zebrafish larva stained with anti-GFP (green) (F'-I'), anti-HuC (red) (F''-I'') and DAPI (blue) (F'''-I'''). Lifeact-eGFP^{+} cells are observed in the olfactory bulb, subpallium (F'), habenula, retina, eminentia thalami, preoptic region, pallium (G'), tectum opticum, hypothalamus (H'), cerebellar plate, and medulla oblongata (I'). Boxed regions are enlarged in panels J to M. Scale Bars: 50 µm.

J-M Enlarged optical sections of the areas boxed in panels (F-I), showing Lifeact-eGFP^{+}/HuC^{+} neurons in the brain parenchyma. Scale bars: 25 µm.

N Schematic representation of the coronal sections of the brain illustrated in F-I, with the forebrain in pink, the midbrain in turquoise, and the hindbrain in peach.

Data information: CeP, cerebellar plate; DT, dorsal thalamus; EmT, eminentia thalami; H, rostral hypothalamus; Ha, habenula; Hc, caudal hypothalamus; MO, medulla oblongata; N, region of the nucleus of medial longitudinal fascicle; M2, migrated posterior tubercular area; M3, migrated area of EmT; OB, olfactory bulb; Oe, olfactory epithelium; P, pallium, Po, preoptic region; PTv, ventral part of posterior tuberculum; Re, retina; S, subpallium; TeO, tectum opticum; T, midbrain tegmentum; dpf, days post-fertilization.

Figure EV1. The *Gpr85* reporter line shows non-proliferating cells expressing *gpr85* in the developing brain mesenchyme, and *Gpr85* is broadly expressed in the post-embryonic developing brain (mapzebrain atlas).

A Confocal imaging of the midbrain ventral region of 3 dpf *gpr85*$^{GAL4/+}$*, Tg(UAS:Lifeact-eGFP)* zebrafish larvae stained with anti-GFP (green), anti-HuC (red), and DAPI (blue). Some

Lifeact-eGFP^{+} cells can be observed in the HuC^{-} neural progenitor/precursor area (white arrowheads). Scale bar: 50 µm.

B Maximum projection confocal images of coronal sections of the brain of 3 dpf *gpr85*$^{GAL4/+}$, *Tg(UAS:Lifeact-eGFP)* zebrafish larvae stained with anti-GFP (green), anti-PCNA (magenta), and DAPI (blue). The box indicates the region enlarged in panel C. Scale bar: 50 µm.

C Higher magnification of the boxed region in panel B, focusing on the ventral telencephalon. None of the PCNA^{+} cells in the progenitor/precursor zone are Lifeact-eGFP^{+} (white arrowheads). Scale bar: 50 µm.

D-G Confocal images of horizontal sections from a 6 dpf *gpr85*$^{GAL4/+}$, *Tg(UAS:Lifeact-eGFP)* zebrafish larva showing Lifeact-eGFP staining in the highlighted anatomical regions. Full dataset is available online on https://mapzebrain.org/atlas/2d (marker: *gpr85*; Shainer *et al*, 2023; Data ref: Shainer *et al*, 2023). Scale bars: 100 µm.

H Confocal image of a coronal section of a 6 dpf *gpr85*$^{GAL4/+}$, *Tg(UAS:Lifeact-eGFP*) zebrafish larva showing Lifeact-eGFP^{+} cells in the habenula. Scale bar: 100 µm.

I Schematic representation of the shown sections through a 6 dpf zebrafish brain, with the forebrain in pink, the midbrain in turquoise, and the hindbrain in peach.

Data information: Ce, cerebellum; dpf, days post fertilization; Ha, habenula; H, hypothalamus; MO, medulla oblongata; OB, olfactory bulb; P, pallium; S, subpallium; TeO, optic tectum; TL, torus longitudinalis.

Figure 2. Cartography of *gpr85* expression in the brain of adult zebrafish.

A Maximum projection confocal images of native Lifeact-eGFP fluorescence in a cleared adult brain hemisphere (sagittal view) from a *gpr85*$^{GAL4/+}$, *Tg(UAS:Lifeact-eGFP)* fish. Scale bar: 500 µm.

B-H' Maximum projection confocal images of brain sections from a *gpr85*$^{GAL4/+}$, *Tg(UAS:GFP-CAAX)* adult zebrafish stained with anti-GFP (green) and DAPI (blue). Sagittal sections of the cerebellum (B-E') with boxes showing regions enlarged in panels C and E, respectively.

Coronal section of the torus longitudinalis (F), with box highlighting the region enlarged in G. Coronal section of the habenula (H, H'). Scale bars: (B, C, E, F, G, H) 50 µm, (D) 500 µm.

Data information: A, anterior; Ce, cerebellum; dpf, days post-fertilization; D, dorsal; Ha, habenula; H, hypothalamus; MO, medulla oblongata; mpf, months post-fertilization; OB, olfactory bulb; P, posterior; Tel, Telecephalum; TeO, optic tectum; TL, torus longitudinalis; V, ventral.

Figure EV2. Cartography of *gpr85* expression in the pituitary, hypothalamus and optic tectum of adult zebrafish.

A-E' Maximum projection confocal images of brain regions from a *gpr85*$^{GAL4/+}$*, Tg(UAS:GFP-CAAX)* adult zebrafish stained with anti-GFP (green) and DAPI (blue). (A) Coronal section of the pituitary gland. The box indicates the region enlarged in panel B. (B) Enlarged view of the region boxed in A. (C-E') Sagittal sections of the optic tectum (C) and the caudal hypothalamus (D). The box in D indicates the regions enlarged in panels E. (E) Enlarged view of the region boxed in D. Scale bars: (A, C, D) 50 µm, (B, E) 25 µm.

Figure 3. Gpr85 is enriched in the pre- and postsynaptic compartments of developing and adult IPL retinal ribbon synapses.

A Maximum projection confocal images of the retina from a *gpr85*$^{GAL4/+}$, *Tg(UAS:GFP-CAAX)* adult zebrafish stained with anti-GFP (green) and DAPI (blue). Scale bar: 50 µm.

B-I'' Confocal images of coronal retinal sections from 6 dpf (B-E'') or 6 mpf (F-H'') *gpr85*$^{GAL4/+}$, *Tg(UAS:zGpr85-eGFP)* zebrafish stained with anti-GFP (green), anti-Ribeye-a (red), and DAPI (blue). (B, F) Larval or adult zGpr85-eGFP^{+} amacrine cell somas and signal within the IPL are shown, with boxed regions enlarged in C-C'' and G-G'', respectively. White arrowheads highlight zGpr85-eGFP signals adjacent to Ribeye^{+} ribbon terminals. (D, H) Larval or adult zGpr85-eGFP^{+}/Ribeye-a^{+} bipolar cell ribbon pre-synaptic terminals are shown, with boxed regions enlarged in E-E'' and I-I'', respectively. White arrowheads show examples of zGpr85-eGFP signal present in Ribeye^{+} ribbon terminals. Scale bars: (B,D) 25 µm, (F, H) 50 µm, (C, E, G, I) 10 µm.

J Electron microscopy coronal view of the structure of 6 dpf retina from *gpr85*$^{GAL4/+}$, *Tg(UAS:zGpr85-mCherry)* zebrafish larvae. Scale bar: 10 µm.

K Enlarged image of the ribbon pre-synaptic terminals (yellow) from the boxed area in panel J. Boxes indicate regions enlarged in panels M and L. Scale bar: 1 µm.

L-M Enlarged images of synaptic boutons from the boxed area in panel K. White arrowheads highlight postsynaptic densities while black arrowheads point to presynaptic vesicles. Scale bars: 200 nm.

N-Q Immunogold labeling of Ribeye (N-P) and mCherry-tagged Gpr85 (Q-S) focusing on the retinal inner plexiform layer from 6 dpf *gpr85*$^{GAL4/+}$, *Tg(UAS:zGpr85-mCherry)* larvae. Dashed yellow lines highlight plasma membranes. Boxes indicate regions enlarged in panels O, P, R, and S. Scale bars: 200 nm.

O-P Enlarged images of the boxed areas in panel N. Ribeye is successfully detected in the IPL and appears clustered near the membrane of bipolar cell terminals. Scale bars: 200 nm.

R-S Enlarged images of the boxed areas in panel Q. mCherry-tagged Gpr85 appears clustered near plasma membranes in the IPL. Scale bars: 200 nm.

Data information: dpf, days post fertilization; mpf, months post fertilization; ONL, outer nuclear layer; OPL, outer plexiform layer; INL, inner nuclear layer; GCL ganglion cell layer.

Figure 4. Gpr85 is enriched at the level of excitatory and inhibitory synaptic inputs of *gpr85*-expressing neurons throughout the developing and adult brain.

A Confocal images of coronal brain sections from 6 dpf *gpr85*$^{GAL4/+}$, *Tg(UAS:zGpr85-mCherry, UAS:FinGR(PSD)-GFP)* larvae stained with anti-GFP (green), anti-mCherry (red), and DAPI (blue). White arrowheads show examples of zGpr85-mCherry signal localized at the level of PSD^{+} excitatory synapses in the telencephalon and optic tectum. Scale bar: 10 µm.

B Confocal images of coronal brain sections from 6 mpf *gpr85*$^{GAL4/+}$, *Tg(UAS:zGpr85-mCherry, UAS:FinGR(PSD)-GFP)* adult zebrafish stained with anti-GFP (green), anti-mCherry (red) and DAPI (blue). White arrowheads show examples of zGpr85-mCherry signal

localized at the level of PSD$^+$ excitatory synapses in the indicated brain regions. Scale bar: 10 µm.

C Confocal images of coronal brain sections from 6 dpf *gpr85*$^{GAL4/+}$, *Tg(UAS:zGpr85-eGFP, UAS:FinGR(GPHN)-mCherry)* larvae stained with anti-GFP (green), anti-mCherry (red), and DAPI (blue). White arrowheads highlight examples of zGpr85-eGFP signal present at the level of the GPHN$^+$ inhibitory synapses in the telencephalon and optic tectum. Scale bar: 10 µm.

D Confocal images of coronal brain sections from 6 mpf *gpr85*$^{GAL4/+}$, *Tg(UAS:zGpr85-eGFP, UAS:FinGR(GPHN)-mCherry)* adult zebrafish stained with anti-GFP (green), anti-mCherry (red) and DAPI (blue). White arrowheads highlight examples of zGpr85-eGFP signal present at the level of the GPHN$^+$ inhibitory synapses of the indicated brain regions. Scale bar: 10 µm.

Data information: dpf, days post fertilization; mpf, months post fertilization.

Figure 5. scRNAseq analysis of eGFP$^+$ sorted cells from adult *gpr85*$^{GAL4/+}$ and *gpr85*$^{GAL4/GAL4}$, *Tg(UAS:lifeact-eGFP)* dissociated brains reveals changes in gene expression related to neuronal activity.

A Experimental strategy for assessing transcriptomic changes in Gpr85-expressing cells from the Gpr85-deficient adult brain. GFP+ cells were sorted from *gpr85*$^{GAL4/+}$ (Ctl) and *gpr85*$^{GAL4/GAL4}$ (KO), *Tg(UAS:lifeact-eGFP)* dissociated brain (cell sorting strategy shown with 10,000 events per condition). The right panel shows the UMAPs of cells from the Ctl and KO conditions (n = 4219 cells and n = 3341 cells, respectively) after filtering and clustering.

B UMAPs of Ctl and KO cells merged, displaying expression of the UAS:lifeact-eGFP transgene, *gpr85*, the two pan-neuronal markers *elavl3* and *rbfox3a*, as well as the expression of the granule cell markers, vsnl1a and pde1a.

C Table of the most up- and down-regulated genes within the isolated cerebellar clusters (0 to 6) in the KO condition, with a minimal fold change of two and an adjusted p-value < 10^{-4}, expressed by at least 6% of the cells.

D Violin plots of selected differentially expressed genes (DEGs) with a minimal fold change of 1.4 and an adjusted p-value < 10^{-4}. All genes referenced are upregulated (mean represented by the dots). Upper panel: genes documented as immediate early genes. Intermediate panel: selection of genes related to calcium-dependent exocytosis. Lower panel: selection of genes encoding channels related to neuronal excitability/activity (voltage-dependent channels: *clcn2a*, *cacna1ba*, *kcnh3*, *cacng8b*; Na^+/K^+ ATPase subunits: *atp1a3b*, *atp1b1b*, *atp1a1a.1*, *atp1b2a*, *syn2b*).

E UMAPs of *npas4a*, *chga* and *atp1b2a* expression in Ctl and KO conditions, respectively.

Figure EV3. scRNAseq supplementary: clustering markers.

A Heatmap of the top 5 markers for each individual cluster. All cells are represented.

B Violin plots of documented markers used for the identification of the different clusters.

C UMAPs of the Ctl and KO cells merged, displaying the expression of key cerebellar markers used to discriminate eurydendroid, Purkinje, stellate, and Golgi cells.

Figure 6. Gpr85-KO impacts adult cerebellar GCs electrophysiological properties and larval light-induced startle response.

A Schematic representation of the experimental setup for recording the electrophysiological properties of adult gpr85-expressing cerebellar GCs *ex vivo*. Cerebellar horizontal sections (220 µm) were prepared, and GCs were identified based on GFP fluorescence. Recordings were made in cell-attached and whole-cell voltage clamp configurations. The chart illustrates the percentage of GCs in cell-attached configuration that exhibited or not spontaneous activity.

B Quantification of GCs spontaneous activity in a cell-attached configuration (firing patterns are shown, as well as the firing rates measured over a 60-second recording (*gpr85*$^{GAL4/+}$, n = 13 vs *gpr85*$^{GAL4/GAL4}$, n = 15, *, p = 0.0347, unpaired t-test with Welch's correction).

C Quantification of GCs passive properties (membrane capacitance, Cm; membrane resistance, Rm; membrane time constant, τ) in a whole-cell voltage clamp configuration (*gpr85*$^{GAL4/+}$, n = 26 vs *gpr85*$^{GAL4/GAL4}$, n = 25; Cm, ns, p = 0.9132; τ, ns, p = 0.1724; Mann Whitney tests; Rm, *, p = 0.0113, unpaired t-test with Welch's correction).

D Schematic representation of the experimental setup for assessing spontaneous locomotor activity. The locomotor activity of larvae was recorded for 20 minutes in the dark after a 5-minute adaptation period.

E Quantification of the distance swum by 6 dpf Gpr85-KO larvae compared to siblings over 20 minutes in the dark (*gpr85*$^{\Delta4/\Delta4}$, n = 69 vs siblings, n = 210, p = 0.36; and *gpr85*$^{GAL4/GAL4}$, n = 77, vs siblings, n = 190, p = 0.94, ns, not significant, Mann Whitney tests).

F Schematic representation of the experimental setup for measuring light-induced startle responses. Larvae were recorded after a 5-minute habituation period. Spontaneous locomotor activity in the dark was recorded for 10 seconds as a baseline, followed by continuous light stimulation. The startle response was recorded within the first second following light onset.

G The startle response was observed in controls as a significant increase in the distance swum following light onset (n = 210 siblings of *gpr85*$^{\Delta4/\Delta4}$ mutants, dark vs startle response, *, p = 0.02; n = 247 siblings of *gpr85*$^{GAL4/GAL4}$ mutants, dark vs startle response, ****, p<0.0001, Wilcoxon matched-paired signed-rank tests). The startle response was significantly more pronounced in *gpr85*-deficient animals compared to controls (n = 80 *gpr85*$^{\Delta4/\Delta4}$ mutants vs siblings, *, p = 0.015; n = 83 *gpr85*$^{GAL4/GAL4}$ mutants vs siblings, *, p = 0.011, Mann Whitney tests).

Data information: Ce, cerebellum; GCL, granule cell layer; SLA, spontaneous locomotor activity; SR, startle response. Data are presented as mean ± SEM (B, C) or SD (E, G).

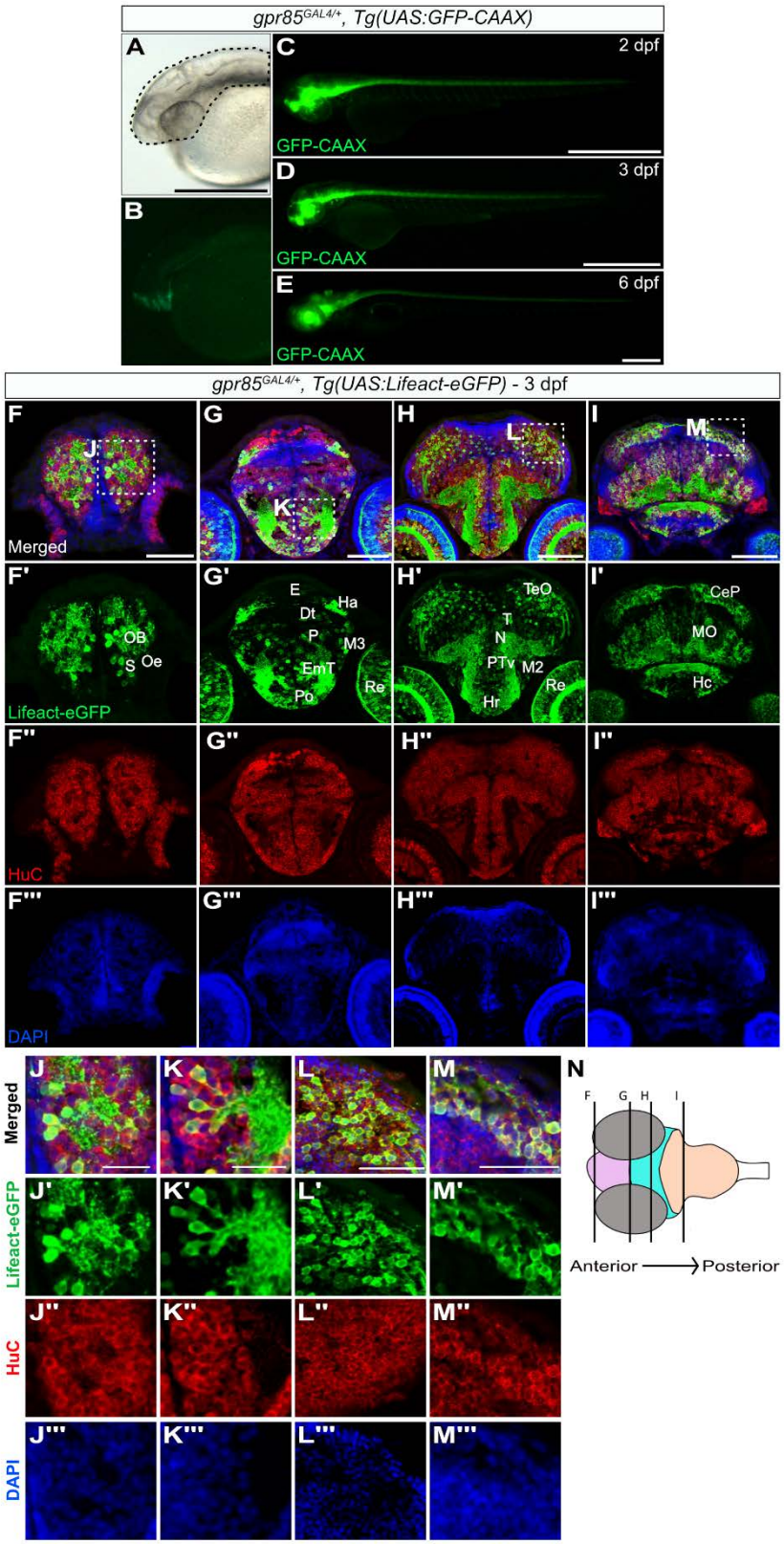
gpr85GAL4/+, Tg(UAS:GFP-CAAX)
A
B
C
2 dpf
GFP-CAAX
D
3 dpf
GFP-CAAX
E
6 dpf
GFP-CAAX
gpr85GAL4/+, Tg(UAS:Lifeact-eGFP) - 3 dpf
F
G
H
I
J
K
L
M
Merged
F'
G'
H'
I'
OB
S
Oe
E
Ha
Dt
P
M3
EmT
Po
Re
TeO
T
N
PTv
M2
Hr
CeP
MO
Hc
Lifeact-eGFP
F''
G''
H''
I''
HuC
F'''
G'''
H'''
I'''
DAPI
Merged
Lifeact-eGFP
HuC
DAPI
N
F
G
H
I
Anterior
Posterior

Figure 1

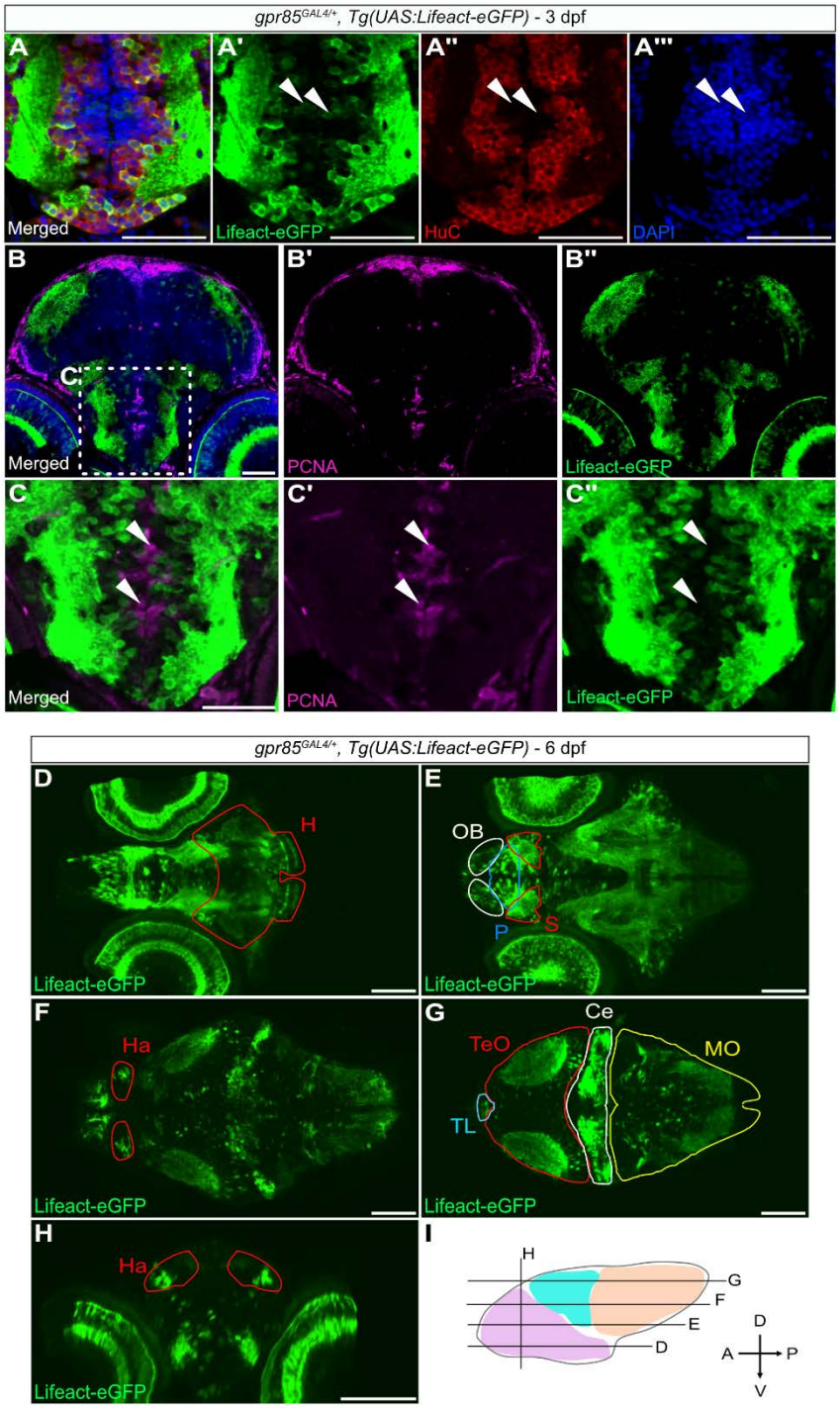

1

2 **Figure EV1**

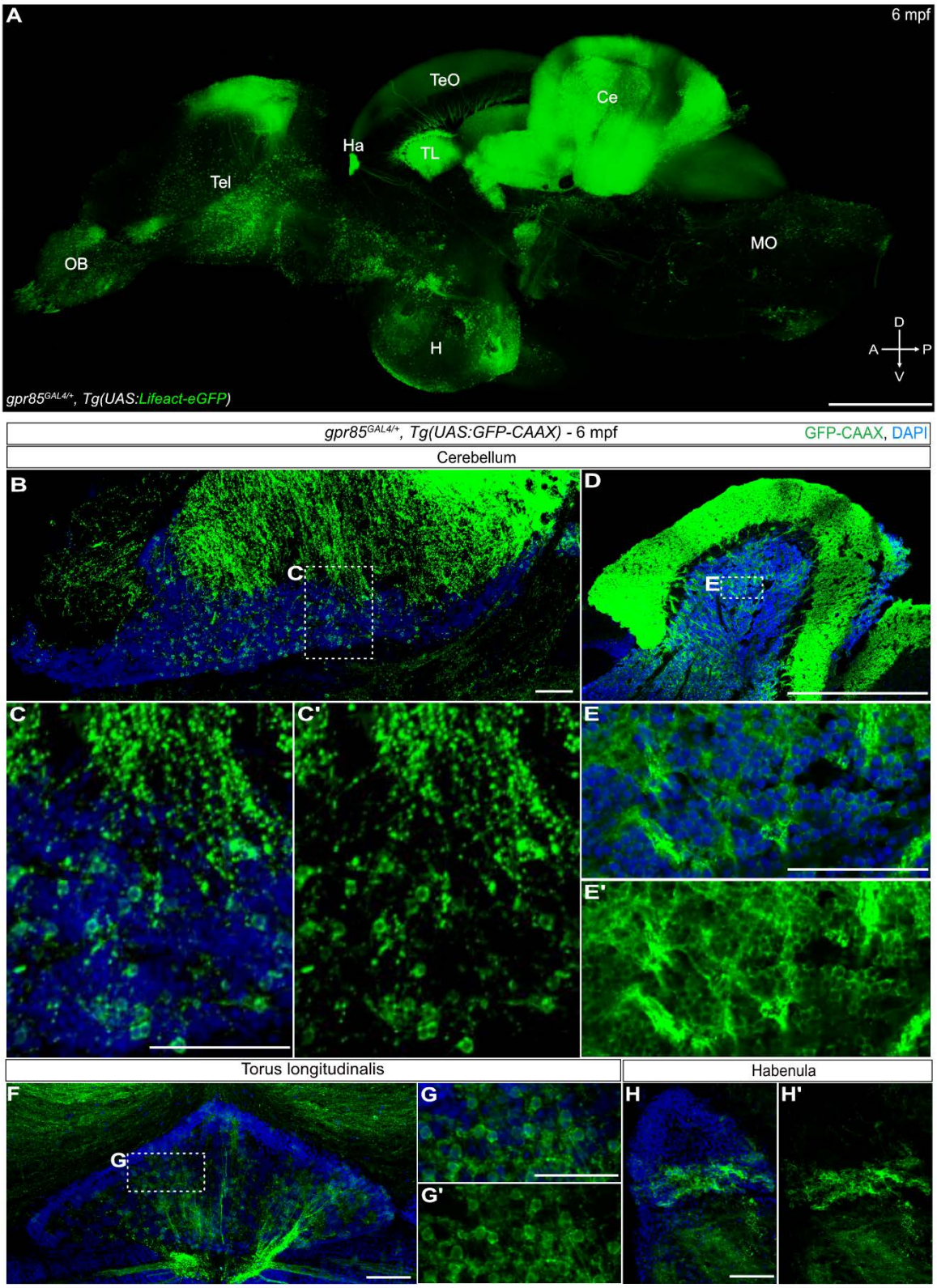
A
6 mpf
TeO
Ce
Ha
TL
Tel
OB
MO
H
D
A
P
V
gpr85GAL4/+, Tg(UAS:Lifeact-eGFP)
gpr85GAL4/+, Tg(UAS:GFP-CAAX) - 6 mpf
GFP-CAAX, DAPI
Cerebellum
B
C
D
E
C
C'
E
E'
Torus longitudinalis
Habenula
F
G
G
G'
H
H'

Figure 2

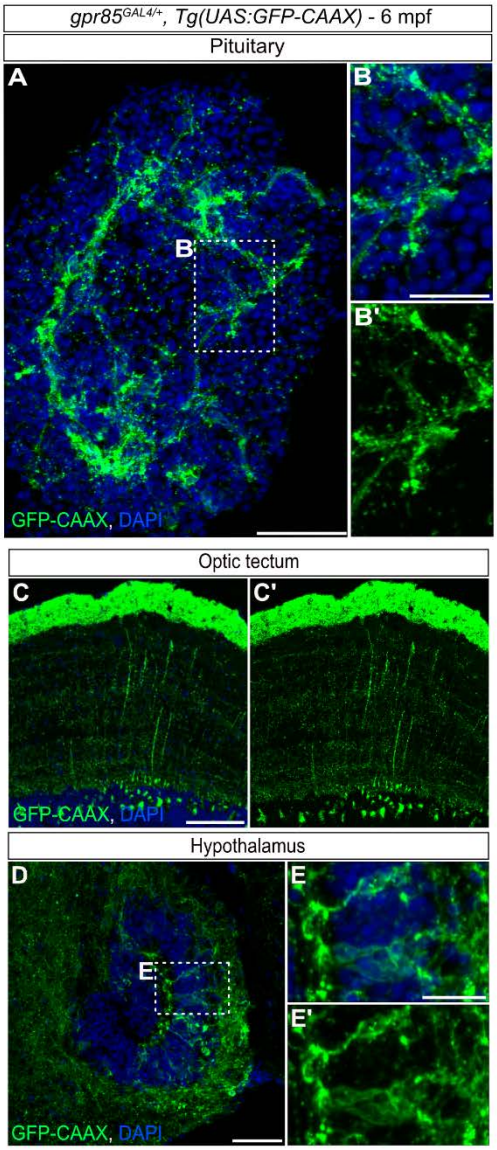
gpr85GAL4/+, Tg(UAS:GFP-CAAX) - 6 mpf
Pituitary
A
B
B
B'
GFP-CAAX, DAPI
Optic tectum
C
C'
GFP-CAAX, DAPI
Hypothalamus
D
E
E
E'
GFP-CAAX, DAPI

Figure EV2

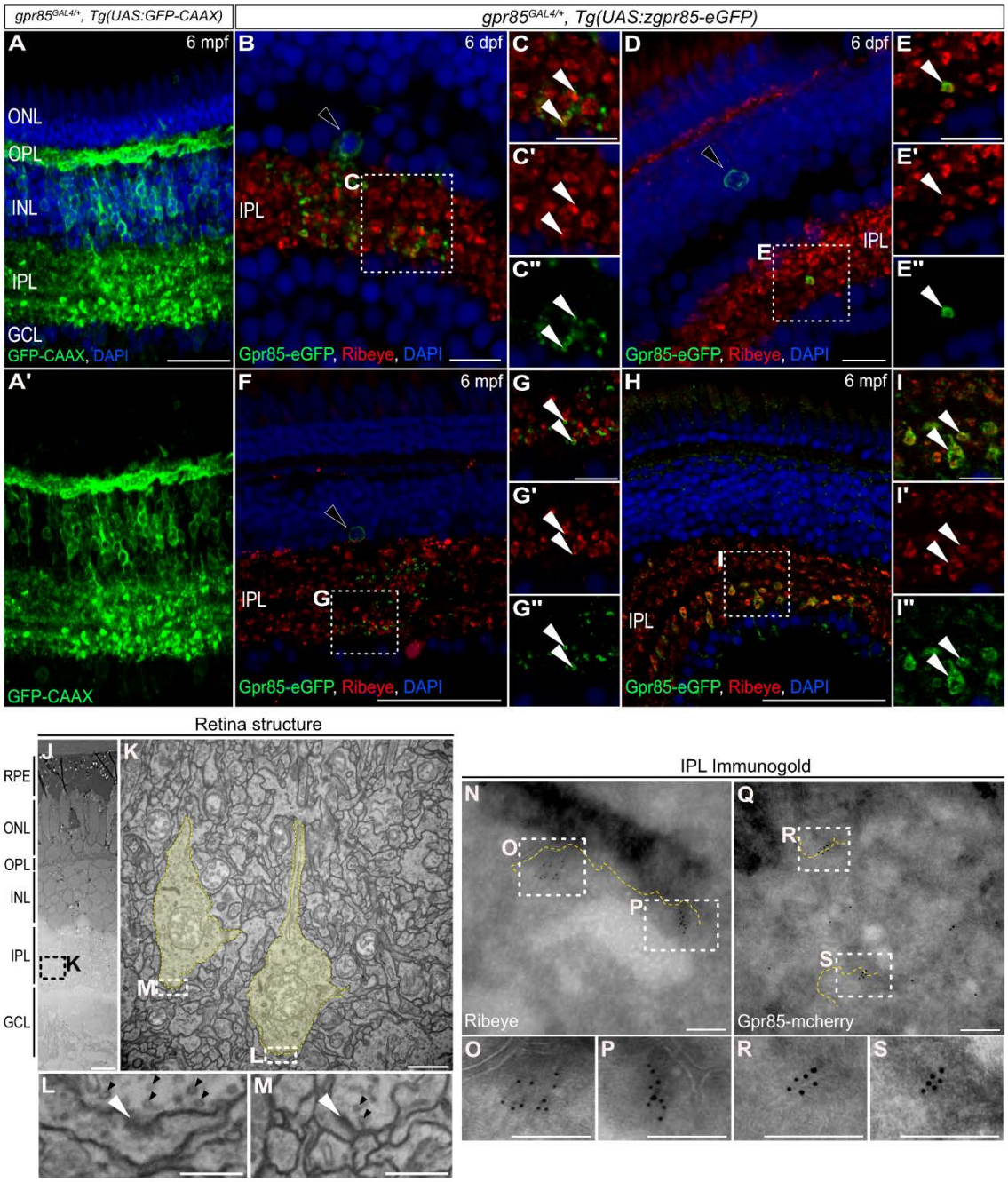
gpr85GAL4/+, Tg(UAS:GFP-CAAX)
gpr85GAL4/+, Tg(UAS:zgpr85-eGFP)
A
6 mpf
ONL
OPL
INL
IPL
GCL
GFP-CAAX, DAPI
B
6 dpf
IPL
C
Gpr85-eGFP, Ribeye, DAPI
C'
C''
D
6 dpf
E
IPL
Gpr85-eGFP, Ribeye, DAPI
E'
E''
A'
GFP-CAAX
F
6 mpf
IPL
G
Gpr85-eGFP, Ribeye, DAPI
G'
G''
H
6 mpf
I
IPL
Gpr85-eGFP, Ribeye, DAPI
I'
I''
Retina structure
RPE
ONL
OPL
INL
IPL
GCL
J
K
M
L
IPL Immunogold
N
O
P
Ribeye
Q
R
S
Gpr85-mcherry

Figure 3

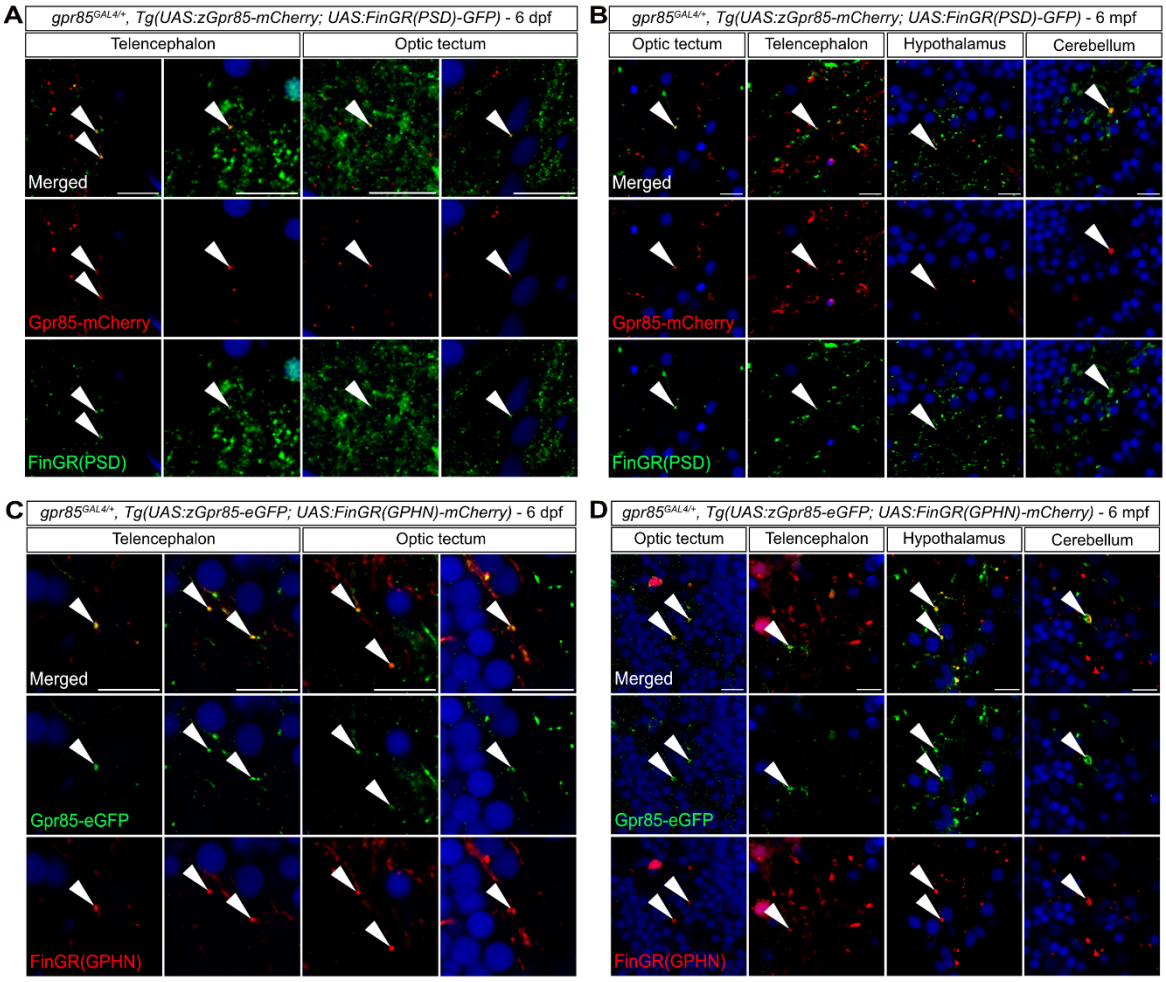
A
gpr85GAL4/+, Tg(UAS:zGpr85-mCherry; UAS:FinGR(PSD)-GFP) - 6 dpf
Telencephalon
Optic tectum
Merged
Gpr85-mCherry
FinGR(PSD)
B
gpr85GAL4/+, Tg(UAS:zGpr85-mCherry; UAS:FinGR(PSD)-GFP) - 6 mpf
Optic tectum
Telencephalon
Hypothalamus
Cerebellum
Merged
Gpr85-mCherry
FinGR(PSD)
C
gpr85GAL4/+, Tg(UAS:zGpr85-eGFP; UAS:FinGR(GPHN)-mCherry) - 6 dpf
Telencephalon
Optic tectum
Merged
Gpr85-eGFP
FinGR(GPHN)
D
gpr85GAL4/+, Tg(UAS:zGpr85-eGFP; UAS:FinGR(GPHN)-mCherry) - 6 mpf
Optic tectum
Telencephalon
Hypothalamus
Cerebellum
Merged
Gpr85-eGFP
FinGR(GPHN)

Figure 4

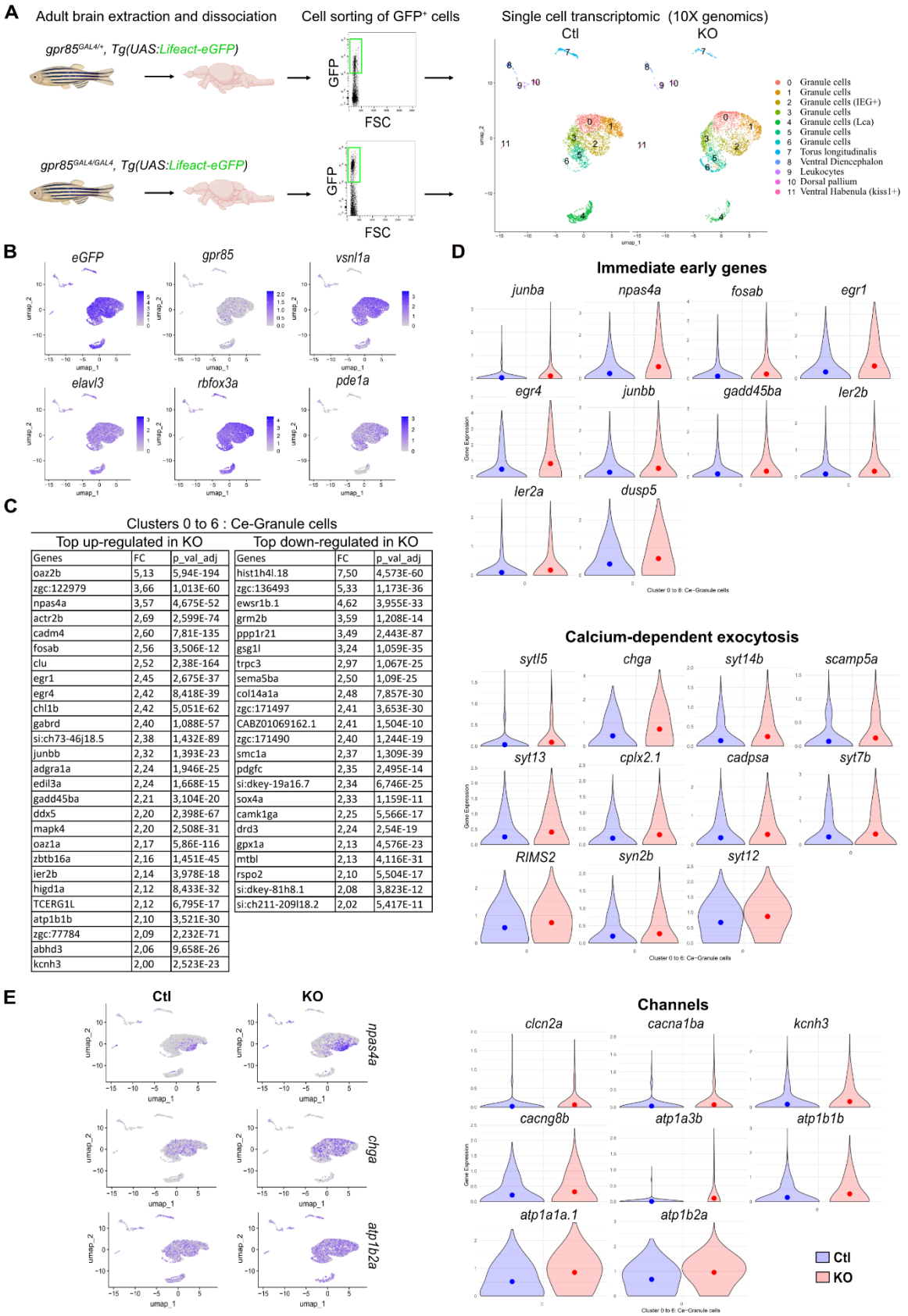

Genes	FC	p_val_adj
oaz2b	5,13	5,94E-194
zgc:122979	3,66	1,013E-60
npas4a	3,57	4,675E-52
actr2b	2,69	2,599E-74
cadm4	2,60	7,81E-135
fosab	2,56	3,506E-12
clu	2,52	2,38E-164
egr1	2,45	2,675E-37
egr4	2,42	8,418E-39
chl1b	2,42	5,051E-62
gabrd	2,40	1,088E-57
si:ch73-46j18.5	2,38	1,432E-89
junbb	2,32	1,393E-23
adgra1a	2,24	1,946E-25
edil3a	2,24	1,668E-15
gadd45ba	2,21	3,104E-20
ddx5	2,20	2,398E-67
mapk4	2,20	2,508E-31
oaz1a	2,17	5,86E-116
zbtb16a	2,16	1,451E-45
ier2b	2,14	3,978E-18
higd1a	2,12	8,433E-32
TCERG1L	2,12	6,795E-17
atp1b1b	2,10	3,521E-30
zgc:77784	2,09	2,232E-71
abhd3	2,06	9,658E-26
kcnh3	2,00	2,523E-23

Genes	FC	p_val_adj
hist1h4l.18	7,50	4,573E-60
zgc:136493	5,33	1,173E-36
ewsr1b.1	4,62	3,955E-33
grm2b	3,59	1,208E-14
ppp1r21	3,49	2,443E-87
gsg1l	3,24	1,059E-35
trpc3	2,97	1,067E-25
sema5ba	2,50	1,09E-25
col14a1a	2,48	7,857E-30
zgc:171497	2,41	3,653E-30
CABZ01069162.1	2,41	1,504E-10
zgc:171490	2,40	1,244E-19
smc1a	2,37	1,309E-39
pdgfc	2,35	2,495E-14
si:dkey-19a16.7	2,34	6,746E-25
sox4a	2,33	1,159E-11
camk1ga	2,25	5,566E-17
drd3	2,24	2,54E-19
gpx1a	2,13	4,576E-23
mtbl	2,13	4,116E-31
rspo2	2,10	5,504E-17
si:dkey-81h8.1	2,08	3,823E-12
si:ch211-209l18.2	2,02	5,417E-11

Figure 5

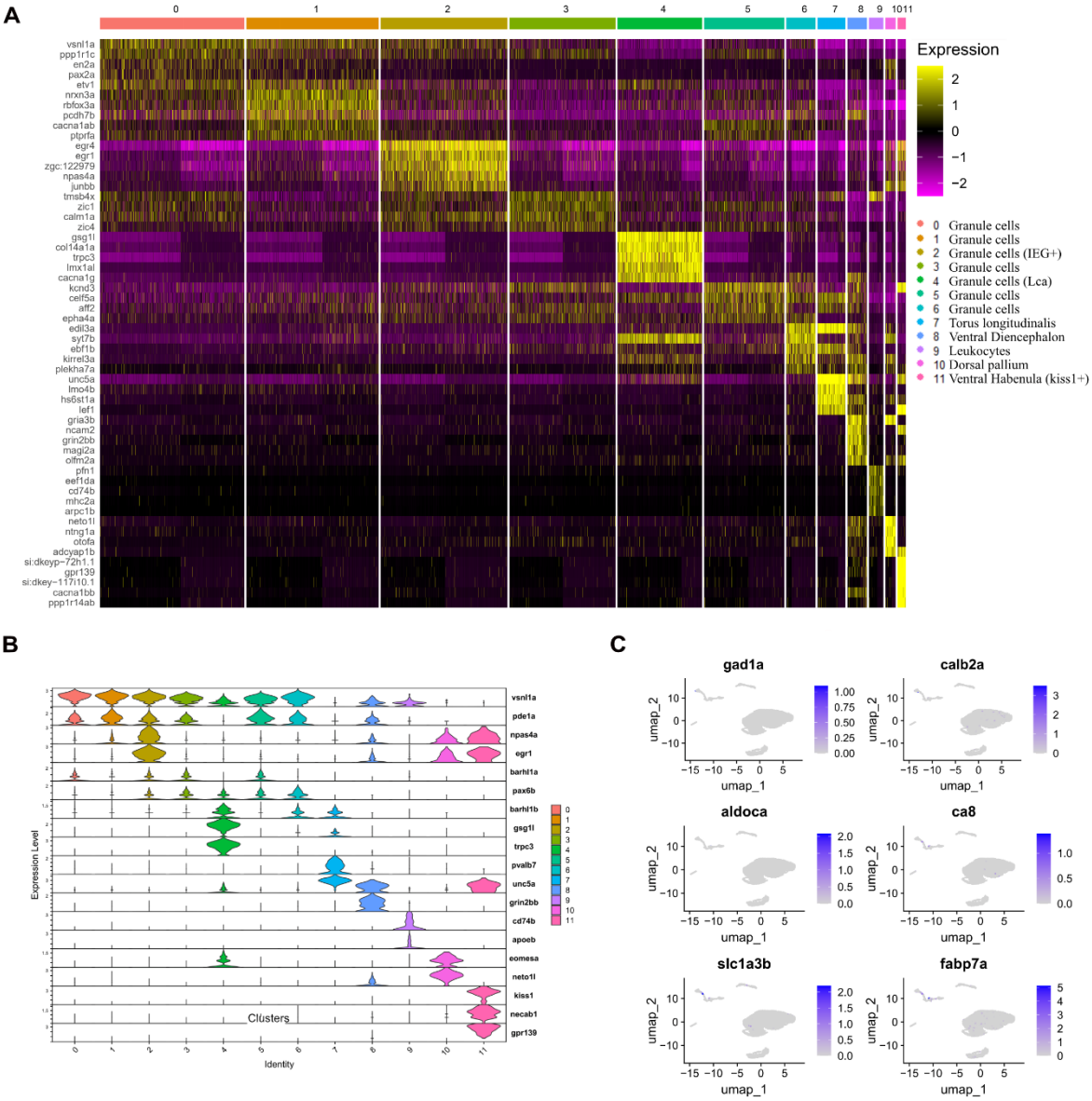

1

2 **Figure EV3**

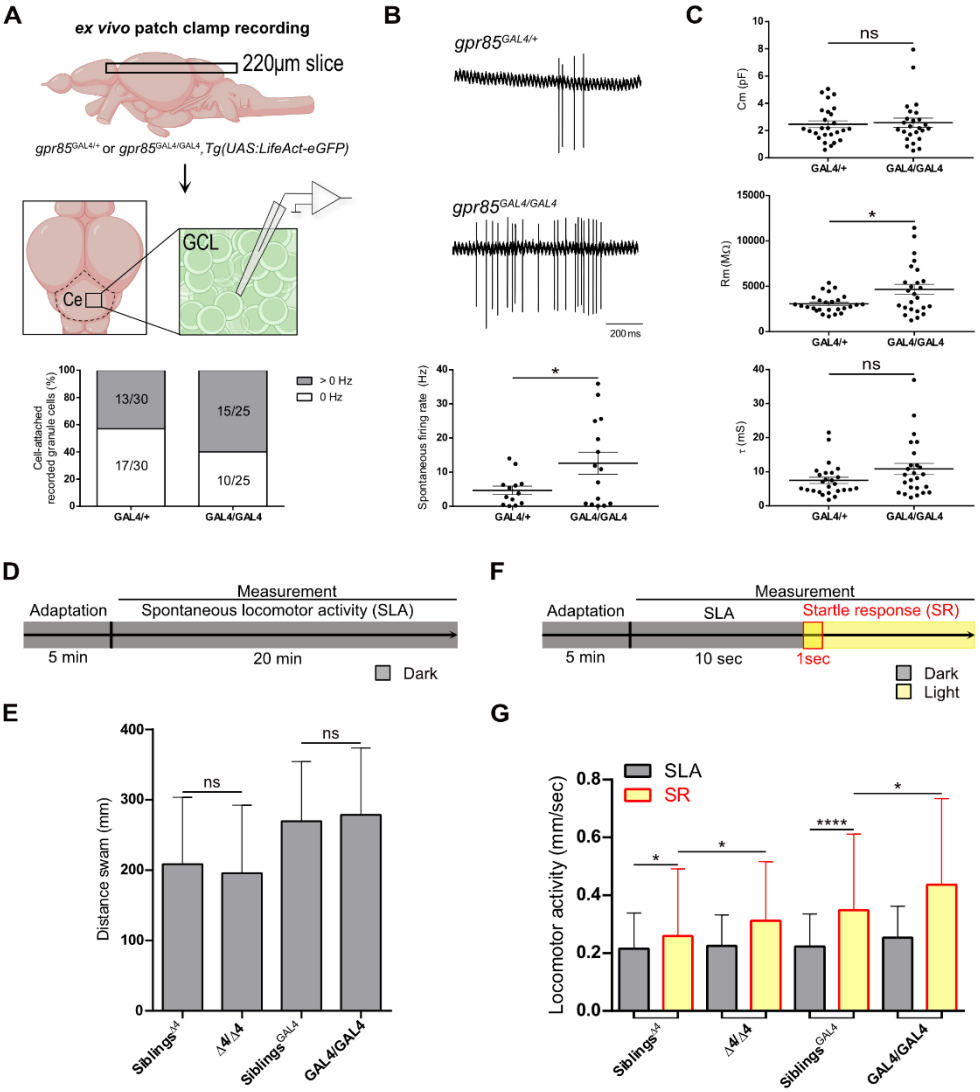
A
ex vivo patch clamp recording
220µm slice
gpr85GAL4/+ or gpr85GAL4/GAL4, Tg(UAS:LifeAct-eGFP)
GCL
Ce
Cell-attached recorded granule cells (%)
13/30
17/30
15/25
10/25
> 0 Hz
0 Hz
GAL4/+
GAL4/GAL4
B
gpr85GAL4/+
gpr85GAL4/GAL4
200 ms
Spontaneous firing rate (Hz)
C
Cm (pF)
Rm (MΩ)
τ (mS)
ns
D
Adaptation
Measurement
Spontaneous locomotor activity (SLA)
5 min
20 min
Dark
E
Distance swam (mm)
Siblings14
Δ4/Δ4
SiblingsGAL4
GAL4/GAL4
F
Adaptation
Measurement
SLA
Startle response (SR)
5 min
10 sec
1sec
Dark
Light
G
Locomotor activity (mm/sec)
SLA
SR

1

2 **Figure 6**